# Design and Performance of Insect-Scale Flapping-Wing Vehicles

Thesis advisor

**Robert J. Wood**

Author

**John Peter Whitney**

**Design and Performance of Insect-Scale Flapping-Wing Vehicles**

# Abstract

Micro-air vehicles (MAVs)—small versions of full-scale aircraft—are the product of a continued path of miniaturization which extends across many fields of engineering. Increasingly, MAVs approach the scale of small birds, and most recently, their sizes have dipped into the realm of hummingbirds and flying insects. However, these non-traditional biologically-inspired designs are without well-established design methods, and manufacturing complex devices at these tiny scales is not feasible using conventional manufacturing methods. This thesis presents a comprehensive investigation of new MAV design and manufacturing methods, as applicable to insect-scale hovering flight. New design methods combine an energy-based accounting of propulsion and aerodynamics with a one degree-of-freedom dynamic flapping model. Important results include analytical expressions for maximum flight endurance and range, and predictions for maximum feasible wing size and body mass. To meet manufacturing constraints, the use of passive wing dynamics to simplify vehicle design and control was investigated; supporting tests included the first synchronized measurements of real-time forces and three-dimensional kinematics generated by insect-scale flapping wings. These experimental methods were then expanded to study optimal wing

shapes and high-efficiency flapping kinematics. To support the development of high-fidelity test devices and fully-functional flight hardware, a new class of manufacturing methods was developed, combining elements of rigid-flex printed circuit board fabrication with "pop-up book" folding mechanisms. In addition to their current and future support of insect-scale MAV development, these new manufacturing techniques are likely to prove an essential element to future advances in micro-optomechanics, micro-surgery, and many other fields.

# Contents

# Chapter 1

# Introduction

## 1.1 Preface

In his 1844 short story, *The Artist of The Beautiful*, Nathaniel Hawthorne writes of a master watch repairer who is consumed with the idea of building a mechanical butterfly. So fine are the features of his creation, that an errant tremor of the wrist, a moment of distraction, might wipe out a month's work. No matter. It is the act of creation itself that drives him.

It is difficult to tell others, seriously, that you are trying to build and study mechanical insects. You could say there are important applications to be had (people have now seen video feeds from aerial drones flown into the maw of a destroyed nuclear reactor station—usually this is a convincing story), or that it provides a vehicle for the study and understanding of real insects. This last point might be true, and a few results from this thesis breed enormous temptation for speculation in this regard, but such an exercise is, almost always, very dangerous. I hope that warnings within are

enough to at suppress these temptations until a more serious approach on the matter is made.

The contributions to our understanding of aerodynamics and insect flight made by this thesis are minor and technical in nature, but some of the tools developed will be very useful for continued exploration. The design methods I developed for flapping-wing mechanical insects are likely more significant, and while not in design or practice an attempt to understand the diversity of insect form and function, a few results might indicate new ways of approaching that issue. The manufacturing techniques I developed (with great inspiration from and close collaboration with my colleague, P. S. Sreetharan) have been the unexpected jewel of these efforts. The wide success of our manufacturing work and its promising future renew me to continue exploring new things for no other reason than *because they are interesting and challenging.*

## 1.2 Flying insects

Insects fly in a manner distinctly different than fixed-wing aircraft ("planes") and with only passing similarity to rotary-wing aircraft ("helicopters"). Figure 1.1 presents a range of species (hummingbirds are commonly studied alongside insects due to strong biomechanical similarities). The smallest flying insects, thrips, may be smaller than 1 millimeter in length, while several large moths (and many hummingbirds) are 10 centimeters or larger in size. Reynolds numbers extend from as low as 10 up to the low 10000s. In spite of a wide diversity of size, shape, and life cycle, flying insects share a relatively similar flight apparatus. Two (or perhaps four) wings stroke back and forth, turning over at the ends of each stroke and meeting the

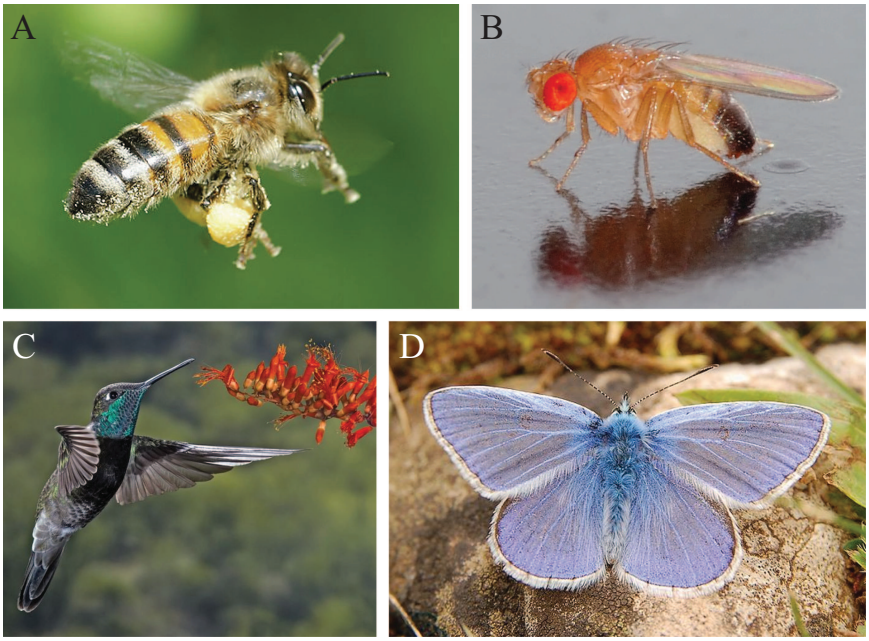


Figure 1.1: (A) *Apis mellifera* "Western honey bee" (image: Hans Hillewaert). (B) *Drosophila melanogaster* "Fruit fly" (image: Andre Karwath). (C) *Eugenes fulgens* "Magnificent hummingbird". (D) *Polyommatus icarus* "Common blue" (image: Luc Viatour).

air, mid-stroke, at a rather large "angle-of-attack" of around 45 degrees. This wing motion is quite apart from human-made aircraft.

### 1.2.1 Flapping kinematics

The flapping cycle is divided by convention into the "upstroke" and "downstroke"; the former is the semiperiod when the wings are drawn from their full extent forward (toward the anterior), back (and frequently up as well) to their most posterior. The forward-backward flapping angle, here denoted $\phi$, is projected onto the mean stroke plane and measured from the plane extending laterally and normal to the anterior-posterior axis. The wings rotate or "pitch" about their proximal-distal axis with an angle $\psi$, and the axis of rotation may deviate out-of-plane with an angle $\theta$. These


Figure 1.2: Conventions for flapping semiperiods.

angles are measured relative to either a reference rigid plane attached to the wing, or, alternatively, the instantaneous mean wing plane (it need not remain flat and rigid). Although there is much variation between insect species, flapping kinematics are generally similar in shape, with $\max(\phi) > \max(\psi) > \max(\theta)$ in most cases. A review of the detailed variations in flapping kinematics, and associated aerodynamic effects, can be found in [14].

The amazing maneuverability of insects derives from an array of flight muscles which directly or indirectly adjust wing motion, allowing exquisite control of flapping kinematics. On the other hand, insect wings and attachment points are flexible, which allows for passive motion and deformation of wings as well. The degree of importance of these effects has been much debated [5, 17, 16]; it is hypothesized that passive wing dynamics reduce the power required to flap the wings by either reducing inertial power consumption, or allowing passive tailoring of wing shape to optimize aerodynamic efficiency.

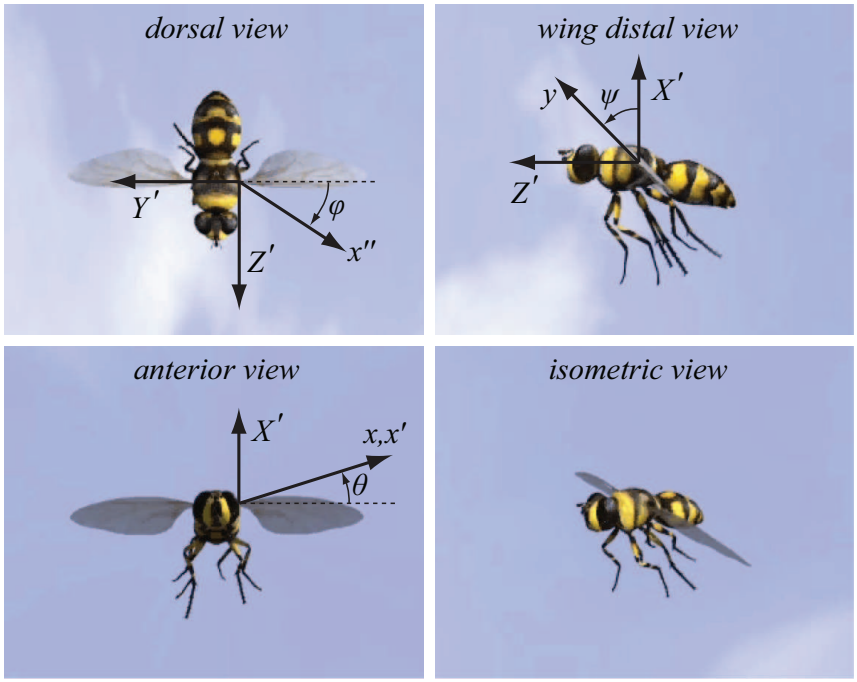


Figure 1.3: Definitions for angular specification of rigid-body wing kinematics.

### 1.2.2 Aerodynamics

The violent motions and large angles of attack seen by an insect wing are quite apart from traditional aircraft. Such conditions, for an aircraft wing, would normally lead to stalled flow and a precipitous drop in efficiency. However, in the case of wings with low aspect ratios, low Reynold number, and revolving (rather than translating) motion, it is frequently found that the wing does not stall and a leading-edge vortex (LEV) grows, but does not separate from the wing. Traditionally this was explained as a "dynamic stall" phenomenon; the idea being that the reciprocating nature of flapping allows the wing to "flip" and reset the vortex before it has a chance to detach. However, recent experiments [28] have observed this effect for wings in continuous revolution (as in a helicopter); the vortex remains attached in spite of steady-state

(albeit revolving) motion. Such stability has been ascribed to centrifugal acceleration [28] or to spanwise flow [38]. Whatever the mechanism, insect wings generate a significant amount of lift, and are not subject, in hover, to the usual restrictions on wing angle-of-attack.

Given their scale, measuring insect flight forces directly has always proved challenging. It is relatively straightforward to measure the mean value of a single component of the total aerodynamic force using a precision balance, but measuring time-varying flight forces at a bandwidth exceeding the flapping frequency, and with sufficient resolution has proven very challenging. With the advent of Reynolds-number matching scaled-model experiments [11], our understanding of insect aerodynamics has advanced greatly. In these experiments, a scaled-up model of the wing is flapped using a mechanical drive system while immersed in a tank of high-viscosity oil or other liquid. By carefully selecting the size of the wing, oil viscosity and flapping frequency, it is feasible to match the Reynolds numbers seen by actual insects, but with a much larger magnitude of the aerodynamic forces and with a much lower flapping frequency. This allows the use of standard force transducers, regular-speed video cameras and the use of traditional flow visualization techniques.

The primary downside of scaled-model testing is that inertial forces are not scaled appropriately. The density of oil is almost 1000 times greater than air, so matching the ratio of wing density to fluid density is not possible, even for thickened wings of plate tungsten. Thus, the exploration of wing deformation and passive dynamics is not possible with these experiments.

## 1.3 Flapping-wing micro air vehicles

While insects and aircraft share the use of wings to generate lift, similarities extend much further. Insects use carbohydrates or fats (fuel) to power flight muscles (engines) and their central nervous system (flight controls). Angular accelerations are measured using vibrating halteres (gyroscopes), augmenting visual feedback from compound eyes (cameras). Although these associations seem obvious or quaint, the investigation and understanding of insects is a treasure trove of ideas for MAV designers, particularly with respect to sensing and control strategies. They are a convenient benchmark for aerodynamic performance, efficiency and maneuverability, and provide a motivating existence proof for the development of high-performance MAVs.

The result of this greater understanding of insect flight and improvements in battery energy density have spawned several recent efforts to develop insect-scale flapping-wing MAVs. Efforts to date are primarily concerned with the *feasibility* of these devices, rather than the optimization of their performance or the establishment of general design principles. Investigations have focused on maximizing thrust-to-weight or minimizing power consumption. Work in the design and optimization of *individual* vehicle subsystems include efforts to optimize stroke kinematics, wing shape and compliance, transmission efficiency, and actuator performance. As a result of these efforts, and as evidenced by recent successful prototypes [18][33][29][30][26], development of practical insect-scale flight vehicles is imminent.

As the required technologies mature, there is an increasing need to establish system-level design principles. The design space for these vehicles is very large, and the relationships between design parameters and performance can be complex and

counter-intuitive.—Does minimizing wing loading maximize flight endurance? What impact will the wing size have on the achievable resonant frequency? Is there an optimal flapping frequency? Do larger or smaller vehicles have longer range? Will an optimal design have a large battery mass fraction?—Once the feasibility of achieving hover has been addressed, these and many other design questions rise to our attention.

Fixed-wing and rotary-wing aircraft have almost a century of development behind them. Standardized design principles have been developed for every stage of the design cycle, beginning with the *conceptual design* phase: here, gross vehicle parameters are determined, including estimates of vehicle mass, wing/rotor size, propulsion requirements, and estimates of the mass fractions of each subsystem. An early step in the conceptual design of a fixed-wing aircraft is called *vehicle sizing* [35]. In this process, vehicle performance requirements are plotted against potential choices for thrust-to-weight ratio (T/W) and wing loading (W/S). The minimum weight vehicle that meets all performance requirements is selected. Variations of this method consider fixed propulsion systems or "rubber engine" models that scale with vehicle size. Similar methods exist for helicopter design: rotor tip speed is usually chosen by constraints on rotor stall and flow compression speeds, autogyration requirements, and rotor noise limits [27]. The main rotor is then sized to balance induced and viscous drag losses. In both fixed and rotary vehicle design, accumulated knowledge of past performance informs the designer "what works".

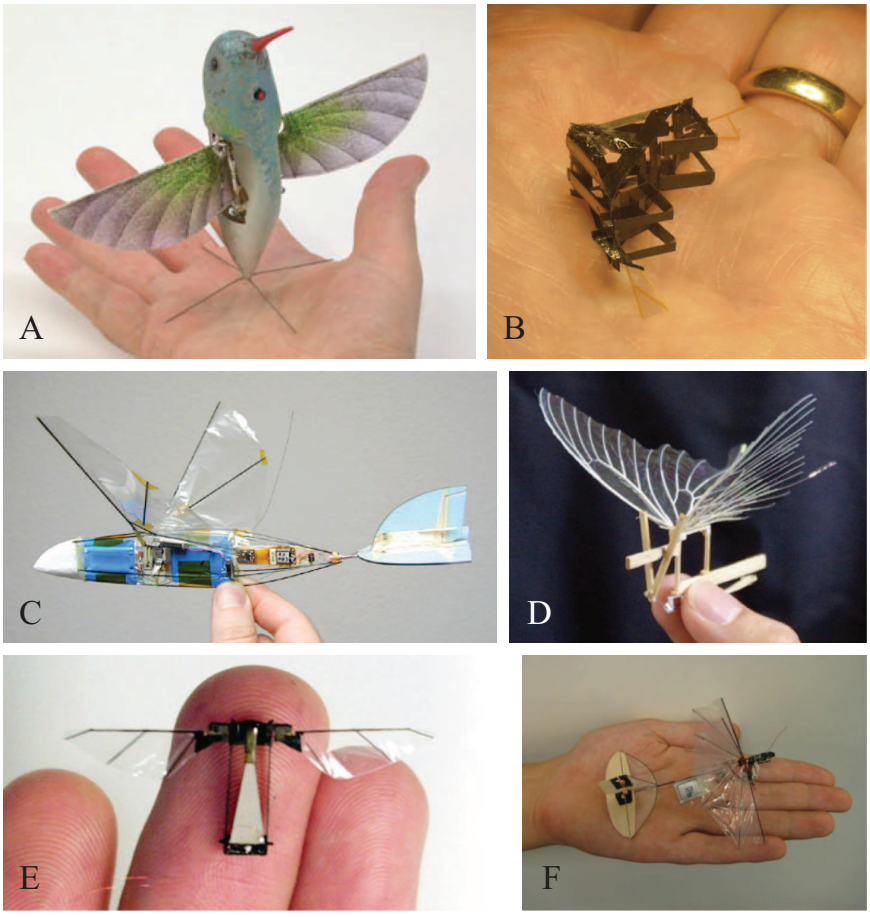


Figure 1.4: (A) Aerovironment "Nano Hummingbird" [26]. (B) Berkeley "Micromechanical Flying Insect" (MFI) [18]. (C) The Caltech/UCLA "Microbat" [33]. (D) Rubber-band powered butterfly by H. Tanaka [44]. (E) Harvard Microrobotic Fly (HMF) [49]. (F) Delft University "delfly micro" [29].

## 1.4 Thesis outline

The task of designing and building a fully-functional insect-scale MAV is daunting. Not only are design methods lacking, but scale and material-appropriate manufacturing methods are not available. The biomechanics of flying insects are incredibly complex, all packaged in a space smaller than a swiss watch. This thesis reports on two parallel and complimentary efforts to attack this problem: the first approach is to extract only the essential mechanical structures and kinematic behaviors required for basic flight function, reducing the manufacturing, assembly and integration challenges. The second approach is to develop improved manufacturing techniques, allowing the construction of three-dimensional electromechanical devices with a level of complexity approaching insects, while meeting challenging mass and material compatibility requirements. In addition to these tasks, this thesis presents a new system-level design approach, adapted from traditional aircraft conceptual design methods to flapping-wing flight.

The following chapters are organized thusly:

**Chapter 2:** Flapping kinematics can be simplified by removing out-of-plane stroke deviations, $\theta(t) = 0$, and by allowing wing rotation, $\psi(t)$, to occur passively, rather than actively. Under this scheme it is possible to develop control torques about all three axes with only two actuators, greatly simplifying the MAV design. However, passive rotation has not been studied experimentally for flapping MAVs. This chapter develops a dynamic model of passive rotation using simple aerodynamic modeling, a rigid-plate approximation for the wing, and a linear model for the compliant wing hinge. These approximations are validated with

the first experiments to combine simultaneous measurement of time-varying forces and three degree-of-freedom angular kinematics of insect-scale flapping wings. To achieve controlled flight with only two actuators, it is necessary to effect intra-period modulation of wing rotation; the efficacy of such a scheme under conditions of passive rotation is experimentally verified.

**Chapter 3:** This chapter presents a new design procedure for flapping-wing vehicle design, establishing conceptual design procedures analogous to fixed-wing and rotary-wing aircraft design. Important results include a prediction for maximum vehicle size and weight in the case of a reciprocating (non-rotational) drive mechanism. An investigation of wing stiffness and moment of inertia yields surprising results with implications for MAV design and (potentially) insect wing morphology. Design insights resulting from vehicle performance optimization are used to direct experiments measuring of the influence of wing aspect ratio, shape, and flapping kinematics on aerodynamic efficiency.

**Chapter 4:** A report on new manufacturing techniques, used not only to make the test devices in chapters 2 and 3, but fully-functional flight vehicles. These techniques are quickly finding use outside of insect-scale MAVs and micro-robotics; a discussion of additional advances in manufacturing are beyond the scope of this thesis, but are presented briefly.

**Chapter 5:** Concluding remarks and a discussion of the trajectory of future research on these topics.

# Chapter 2

# Wing Aeromechanics and Passive Rotation

## 2.1 Introduction

It is almost certain that insects directly exert rotational moments to actively control wing rotation, as they possess musculature so able [14]. However, it is an open question whether or not these muscles provide a significant amount of the power required to flip the wing during "nominal" flapping, or whether they are used only to apply small corrections to the wing's trajectory for control purposes.

For some insects, there is direct evidence of passive rotation from observations of torsional waves that begin at the tip rather than the base of a wing [17]. In addition, aerodynamic estimates have shown that it is possible to achieve rotation purely by passive means for some insects [5], but there is insufficient evidence to make this claim for all insects. For an MAV, relying on passive rotation is not an inevitability,

but a design choice, and one that may significantly reduce the weight and mechanical complexity.

While it is not possible to claim, in general, that passive rotation is the most efficient flapping configuration, its observation in nature and reduced complexity strongly warrant further study. This chapter develops the passive rotation equations of motion and models aerodynamic forces and moments using a blade-element approach. However, the simplifications of the blade-element method present many uncertainties, and experiments are needed to validate its applicability. These experiments must measure and correlate wing forces and kinematics for passively rotating wings.

Experiments in the literature reporting measurements of wing forces and kinematics are numerous. Dickinson [11] used a Reynolds number matched fruit fly (*Drosophila melanogaster*) wing model to measure time varying aerodynamic forces and correlate them to three degree-of-freedom flapping kinematics. Fry [21] and Ristroph [37] used hull reconstruction techniques to measure the three dimensional wing trajectories, and body trajectories, of free-flying *Drosophila*. Taylor [46] used photogrammetric reconstruction to measure complete wing trajectories, including higher order deformations, of locusts (*Schistocerca gregaria*) and hoverflies (*Eristalis tenax*) in a wind tunnel. Graetzel [23], in experiments with *Drosophila*, used a single high-speed video camera to extract the projected flapping angle, while simultaneously measuring vertical forces using a silicon micromachined capacitive force sensor.

The experiments reported here use high-speed video stereophotogrammetry to measure three degree-of-freedom kinematics (flapping, rotation, and out-of-plane motion). Forces are measured, in real-time, using a capacitive-based force sensor. Ar-

tificial wings, with varying torsional compliance, are flapped at different frequencies and amplitudes and allowed to passively rotate. The measured forces and kinematics provide a direct assessment of the blade-element assumptions, and evaluation of the derived equations of motion for several test cases. The quantitative agreement is very good, validating both the wing dynamics model and the continued and expanded use of the experimental setup for studying at-scale flapping wing aerodynamics.

## 2.2 Aeromechanics

### 2.2.1 Wing morphology

Passive rotation characteristics have a strong dependence on the detailed shape and mass distribution of a wing. Natural and artificial wings display great variation in size, planform, material composition, and vein structure [10]. Development of a concise wing parametrization is required. The commonly used definitions by Ellington [15] provide a starting point in the formulation of a complete parametrization.

Figure 2.1 illustrates a generic wing planform. The $x$-axis is aligned with the wing's axis of rotation (torsional axis), where $r$ the radial distance along it. The intersection of the $x$-axis and $y$-axis ($O'$) shall be called the shoulder. Typically the wing root—defined as the most proximal point on the leading edge—is not coincident with the shoulder. The radial distance from the wing root, along the $r'$-axis, is $r'$. The wing root offsets $x_r$ and $y_r$ are labeled in figure 2.1.

The wing length, $R$, is defined here as projected distance along the $r'$-axis from the wing root to the most distal point on the wing. The mean chord, $\bar{c}$, is defined

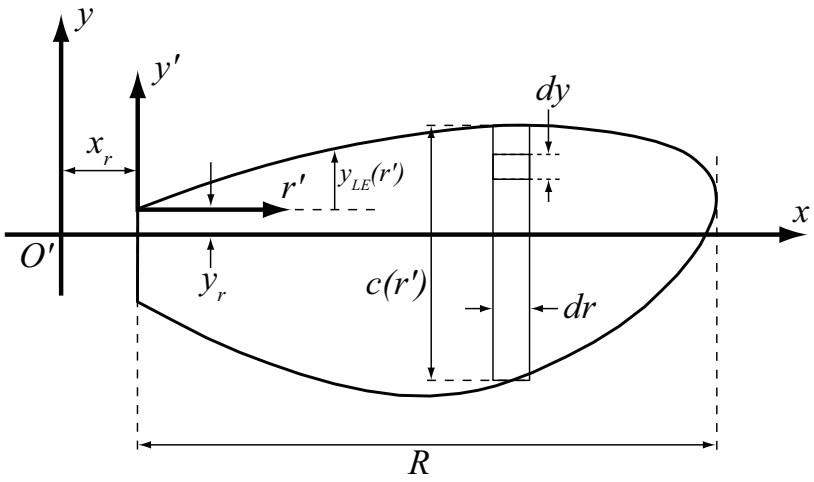


Figure 2.1: Coordinates and dimensions for a generic insect wing planform. Differential elements for radial and chord-wise integration are shown.

as the area of one wing divided by the wing length, $A_w/R$. Radial coordinates may be made nondimensional by $R$ and chordwise coordinates by $\bar{c}$ [15]. Resulting values are radial distance (relative to root) $\hat{r} \equiv r'/R$, chord profile $\hat{c} \equiv c/\bar{c}$, leading edge profile $\hat{y}_{LE} \equiv y_{LE}/\bar{c}$, $x$-root offset $\hat{x}_r \equiv x_r/R$, and $y$-root offset $\hat{y}_r \equiv y_r/\bar{c}$. Passive rotation dynamics depend critically on the shape of the leading edge, as this alters the chordwise location of the center of lift. It is customary to define the wing's aspect ratio as $\mathcal{AR} \equiv R/\bar{c}$. A wing's shape can be fully specified by $R$, $\mathcal{AR}$, $\hat{c}(\hat{r})$, and $\hat{y}_{LE}(\hat{r})$. The choice of $R$ as the sole dimensional parameter was arbitrary—$\bar{c}$ or $A_w$ could serve equally. In addition, the offset parameters $\hat{x}_r$ and $\hat{y}_r$ define the hinge location. Frequently, it is convenient to define $\hat{x}_r = 0$ and fold any radial offset into $\hat{c}(\hat{r})$.

While the wing shape has been fully specified and nondimensionalized, it still contains two arbitrary shape functions, $\hat{c}(\hat{r})$ and $\hat{y}_{LE}(\hat{r})$. This is not a drawback when analysing one specific wing, but it is highly desirable to reduce these functions to a small number of constant parameters which capture only the essential nature of

the wing's shape. This can be accomplished in part by defining radius moments [15] of the form

$$\hat{r}_k^k \equiv \int_0^1 \hat{c}\left(\hat{r}\right) \hat{r}^k \mathrm{d}\hat{r}, \tag{2.1}$$

where the subscript is the moment index and the superscript is an exponent. These parameters can be dimensionalized by multiplying by the wing length. The first-order radius moment, $r_1 = R\hat{r}_1$, is the wing's center of area. Higher order moments describe the area distribution of the wing. For insect wings, there is a strong correlation between $\hat{r}_1$ and $\hat{r}_2$. The analytical relationship

$$\hat{r}_2 = 0.929 \left(\hat{r}_1\right)^{0.732} \tag{2.2}$$

was found to closely fit experimental measurements from insect wings of all shapes and sizes [15]. A beta distribution can be used to reconstruct the non-dimensional wing shape,

$$\hat{c} = \hat{r}^{p-1} \left(1 - \hat{r}\right)^{q-1} / B\left(p, q\right), \tag{2.3}$$

where $B(p, q)$ is the beta function

$$B\left(p, q\right) = \int_0^1 \hat{r}^{p-1} \left(1 - \hat{r}\right)^{q-1} \mathrm{d}\hat{r}. \tag{2.4}$$

If the beta function parameters are chosen as

$$p = \hat{r}_1 \left( \frac{\hat{r}_1 \left(1 - \hat{r}_1\right)}{\hat{r}_2^2 - \hat{r}_1^2} - 1 \right) \tag{2.5}$$

$$q = \left(1 - \hat{r}_1\right) \left( \frac{\hat{r}_1 \left(1 - \hat{r}_1\right)}{\hat{r}_2^2 - \hat{r}_1^2} - 1 \right), \tag{2.6}$$

then the first and second radial moments of (2.3) will be $\hat{r}_1$ and $\hat{r}_2$. Measurements from a wide range of insects, in both species and scale, were made and have been

shown to match this distribution to within 5% [15]. Combined with the relationship given in (2.2), the nondimensional radial area distribution of many insect wings, $\hat{c}(\hat{r})$, can be completely determined from a single constant parameter, the non-dimensional radial location of the wing's center of area, $\hat{r}_1$.

The variety in insect wing shapes are due not just to variations in $\hat{r}_1$ (which ranges from 0.4 to 0.6), but to their many different leading edge profiles. An attempt at parametrizing $\hat{y}_{LE}$ is not known at this time, but would be helpful in analysing the importance of leading edge shape on passive rotation dynamics as well as aerodynamic efficiency in general.

### 2.2.2 Flapping kinematics

Figure 2.2 shows coordinate systems and angles necessary for a basic description of the rigid-wing flapping kinematics of most insects. A left wing is shown close to the end of its downstroke. The $X'Y'Z'$-coordinate frame has its origin $O'$ at the shoulder of the left wing. The $X'$-axis is normal to the mean stroke plane, with the $Y'$-axis pointing in the right lateral direction. The $Z'$-axis points in the ventral direction. The $xyz$-axes are wing-fixed. These are the same axes as those shown in Figure 2.1, though here they are shown offset, next to the wing hinge, for clarity. It is important to place the $xyz$-frame at $O'$ when calculating moments of inertia.

The $x''y''z''$-axes rotate with the flapping angle, $\phi$, defined as the angle between the negative $Y'$-axis and the $x''$-axis, where the axis of rotation is the negative $X'$-axis. The $x'y'z'$-axes (not to be confused with the $r'y'$-axes in figure 2.1) rotate with the flapping angle *and* with the stroke-plane-deviation angle, $\theta$, defined as the angle

between the $x''$-axis and the $x$-axis, where the axis of rotation is the $z''$-axis. The rotation angle, $\psi$, is defined as the angle between the $y'$-axis and $y$-axis, rotating about the $x$-axis. The total angular velocity of the wing is the sum of flapping, deviation, and rotation:

$$\boldsymbol{\omega} = -\dot{\phi}\boldsymbol{e}_{X'} + \dot{\theta}\boldsymbol{e}_{z''} + \dot{\psi}\boldsymbol{e}_x. \tag{2.7}$$

In the wing-bound frame, this becomes

$$\boldsymbol{\omega} = \left(\dot{\psi} - \dot{\phi}\sin\theta\right)\boldsymbol{e}_x + \left(-\dot{\phi}\cos\theta\cos\psi + \dot{\theta}\sin\psi\right)\boldsymbol{e}_y + \left(\dot{\phi}\cos\theta\sin\psi + \dot{\theta}\cos\psi\right)\boldsymbol{e}_z. \tag{2.8}$$

It is useful to define the velocity of the hinge line, $\boldsymbol{v}_h$. The hinge has no radial velocity component,

$$\boldsymbol{v}_h = V_0\boldsymbol{e}_y + W_0\boldsymbol{e}_z, \tag{2.9}$$

and is defined by $\boldsymbol{\omega}_h \times r\boldsymbol{e}_x$, where $\boldsymbol{\omega}_h$ is given by $\boldsymbol{\omega} - \omega_x\boldsymbol{e}_x$. The inertial and virtual mass moments depend (v.i.) on the acceleration of the wing at the hinge, which is given by

$$\begin{aligned}
\dot{\boldsymbol{v}}_h &= \dot{V}_0\boldsymbol{e}_y + \dot{W}_0\boldsymbol{e}_z \\
&= \dot{\boldsymbol{\omega}}_h \times r\boldsymbol{e}_x + \boldsymbol{\omega}_h \times \boldsymbol{v}_h \\
&= r\left(\dot{\omega}_z + \omega_x\omega_y\right)\boldsymbol{e}_y + r\left(-\dot{\omega}_y + \omega_x\omega_z\right)\boldsymbol{e}_z.
\end{aligned} \tag{2.10}$$

Aerodynamic forces and moments are not directly related to the angle of rotation $\psi$, but rather to the angle-of-attack, $\alpha$, which is defined as the angle between the wing chord and the instantaneous local velocity:

$$\alpha = \text{atan2}(-\omega_y, \omega_z). \tag{2.11}$$

This definition gives $\alpha$ a right-hand-rule sign convention relative to the $x$-axis.

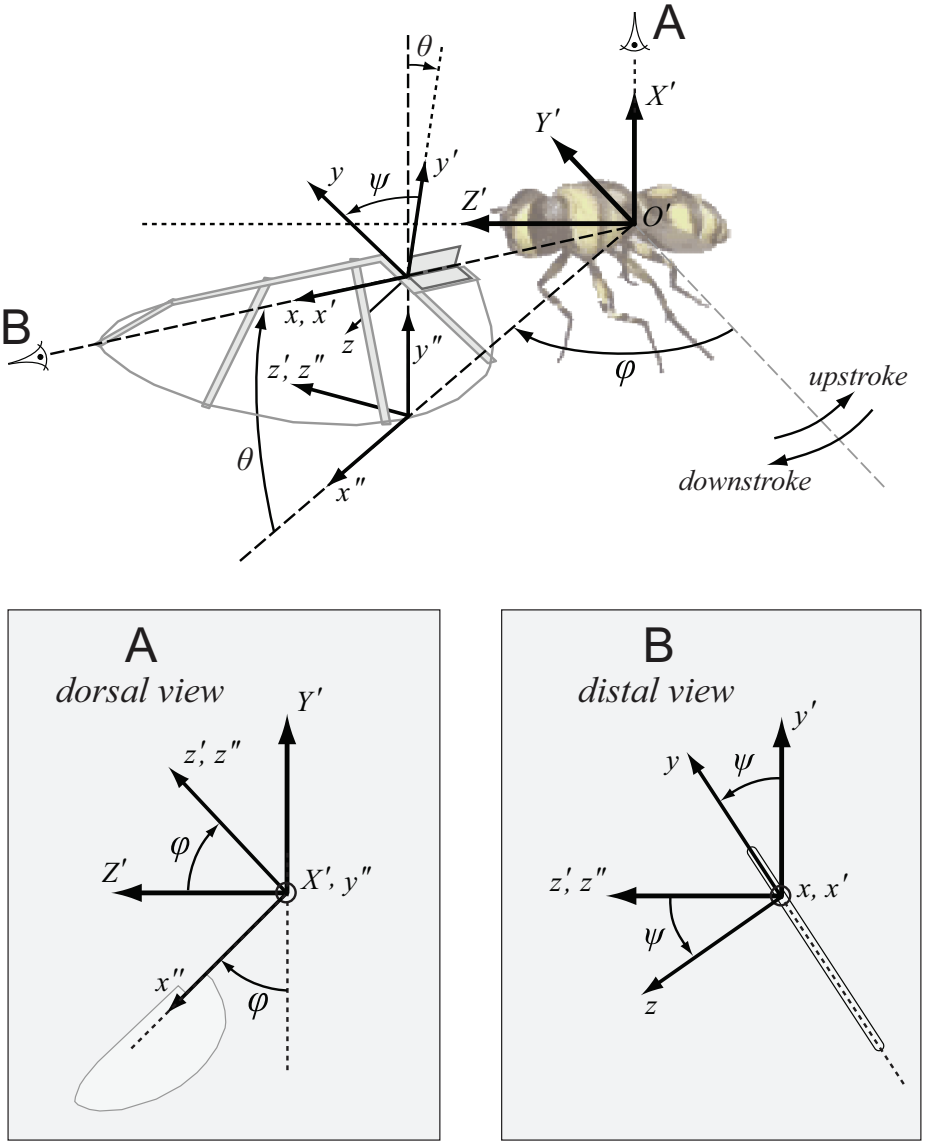


Figure 2.2: Coordinate systems and angles used to specify wing kinematics. All coordinate frames share the same origin, $O'$—they are shown offset here only for clarity.

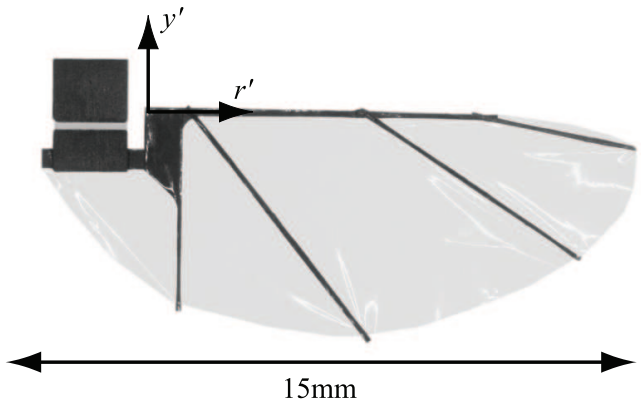


Figure 2.3: A wing of this design is used for experiments performed in this chapter. Wing length is 15mm, measured from "shoulder" to tip. The spars are 80$\mu$m thick carbon fiber, bonded to the wing membrane, 1.5$\mu$m thick polyester film.

### 2.2.3 Wing hinge

For insect-scale flapping-wing robots, passive rotation can be achieved by attaching the wing to the driving spar with an elastic hinge [49]. Figure 2.3 shows a hinge near the base of the wing. The hinge stiffness is controlled by adjusting the geometry and material of a flexible polymer layer sandwiched between rigid structural layers. The rotational stiffness is approximated by that of a linear elastic beam deforming under an external moment,

$$\kappa_h = \frac{E_h t_h^3 w_h}{12 L_h}, \tag{2.12}$$

where $t_h$, $w_h$, and $L_h$ are the thickness, width, and length of the central layer, as shown in figure 2.4, and $E_h$ is the modulus. For all experiments presented here, $L_h$ has sufficient length to prevent the top and bottom structural portions of the hinge from colliding when the wing is maximally rotated.

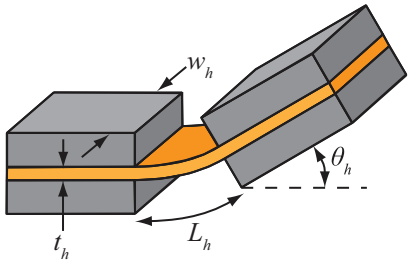


Figure 2.4: Canonical flexure-based wing hinge using a variation of material and geometry to create a compliant joint. Bending stiffness is carefully tailored to optimize passive wing dynamics.

### 2.2.4 Passive rotation equations of motion

Insect wings flex and deform when flapped, as a result of their distributed radial and chord-wise compliance [10]. However, if these deflections are small, assuming rigid body motion of the entire wing is greatly simplifying. With the wing shoulder as an origin, the motion of the wing is entirely rotational. Under these assumptions, the Euler equations are the governing equations of motion. The inertia tensor is defined here as

$$I_{jk} = \int_V \rho_w(\boldsymbol{r}) \left(r^2 \delta_{jk} - x_j x_k\right) \mathrm{d}V, \tag{2.13}$$

where $\rho_w(\boldsymbol{r})$ is the wing density, and $\boldsymbol{r}$ is the displacement vector for the $xyz$-axes. The Euler equation describing rotation about the $x$-axis is

$$\begin{aligned} M_x = I_{xx}\dot{\omega}_x \quad &- \quad (I_{yy} - I_{zz})\,\omega_y\omega_z + I_{xy}\left(\dot{\omega}_y - \omega_x\omega_z\right) + I_{yz}\left(\omega_y^2 - \omega_z^2\right) \\ &+ \quad I_{xz}\left(\dot{\omega}_z + \omega_x\omega_y\right), \end{aligned} \tag{2.14}$$

where $M_x$ is the sum of all external moments about the $x$-axis. For a wing of characteristic thickness $t_w$, assuming a thin wing ($t_w \ll \bar{c}, R$) allows the simplification $I_{xz} = I_{yz} = 0$, and, by the perpendicular axis theorem, $I_{xx} + I_{yy} = I_{zz}$, resulting in

the simplified rotational equation of motion

$$M_x = I_{xx}\left(\dot{\omega}_x + \omega_y\omega_z\right) + I_{xy}\left(\dot{\omega}_y - \omega_x\omega_z\right). \tag{2.15}$$

In the absence of out-of-plane motion ($\theta = \dot{\theta} = 0$), this simplifies to

$$I_{xx}\ddot{\psi} = M_x + I_{xy}\ddot{\phi}\cos\psi + \frac{1}{2}I_{xx}\dot{\phi}^2\sin 2\psi, \tag{2.16}$$

where the kinematic variables have been substituted using 2.8. The net externally applied moment about the $x$-axis, $M_x$, includes aerodynamic moments and the elastic restoring moment from the wing hinge. It would also include direct rotational input torques by the insect or robot.

The second terms on the right-hand sides of 2.16 and 2.15 are the "inertial" moment that results when the wing hinge line does not pass through the center of mass of the wing, helping to "flip" the wing when it is accelerated. With the hinge acceleration given by 2.10, notice in 2.15 that $\dot{\omega}_y - \omega_x\omega_z = -\dot{W}_0/r$. This "inertial flip" term is proportional to the angular acceleration normal to the instantaneous stroke plane.

Given $\phi(t)$, $\theta(t)$, a model for the aerodynamic torque, a model for the elastic wing hinge, and the inertia components $I_{xx}$ and $I_{xy}$, 2.15 is simply integrated in time to determine the passive rotation response, $\psi(t)$.

### 2.2.5 Aerodynamics

A passive rotation simulation requires a model of the aerodynamic forces and moments exerted on the wing. The Reynolds number for flapping flight may be

defined as

$$Re \equiv \frac{\bar{u}\bar{c}}{\nu}, \tag{2.17}$$

where $\bar{u}$ is the mean translational velocity of the wing tip and $\nu$ is the kinematic viscosity of air. The mean translational velocity is given by $2\Phi fR$, where $\Phi$ is the total flapping angular amplitude (peak-to-peak) and $f$ is the flapping frequency. Most insects have a Reynolds number in the 100-1000 range, though some as low as 10 or as high as 10,000 [15].

Flapping kinematics are characterized by large angles-of-attack and high rates of rotation. Massive separation of boundary layers, possible reattachment, and strong vortex shedding at both the leading and trailing edges are possible features of this type of flow. The wing also interacts with its own wake, especially in hover, potentially leading to significant time-dependent aerodynamic forces. Many different aerodynamic effects have been identified, and are reviewed in [38]. Often, experiments attempt to explain the aerodynamics for a single wing at a single operating point, usually with the aim of identifying the important aerodynamic mechanisms for a particular insect species. Recent work [28] reverses this trend; they investigate aerodynamic performance under the systematic variation of (effectively) wing aspect ratio, *Re*, and flapping amplitude.

Two and three-dimensional computational fluid dynamics (CFD) calculations are an alternative to flapping experiments [47, 53, 55]. They provide detailed information on not only the forces and moments, but the structure of the wake and surrounding fluid. Published calculations show good general agreement with experiments. Two-dimensional CFD calculations can now be run fast enough, on supercomputers,

to perform design optimization studies [6]. Performing two-dimensional CFD-based passive rotation design and optimization studies is likely feasible.

Whether aerodynamic force and moment data comes from computation or experiment, it is highly desirable to reduce it to a non-dimensional form. A proper reduction will allow the data to be applied as broadly as possible. The blade element method is a quasi-static technique for applying nondimensional experimental and computational results to similar operating conditions. The success of this method is critically limited by the quality of the force and moment coefficients and its quasi-static assumptions.

### 2.2.6 Blade-element method

Lift and drag coefficients provide a convenient way to apply computational or experimental results to different operating conditions or configurations. The general form of an aerodynamic force coefficient is

$$C_F = \frac{F}{p_{dyn} S}, \tag{2.18}$$

where $F$ is the force in question, $p_{dyn}$ is the dynamic pressure, and $S$ is a reference area. The dynamic pressure is defined as $(1/2)\rho V^2$, where $\rho$ and $V$ are the reference air density and velocity, usually the free stream values. The reference area is usually the area over which the force acts or an area characteristic to the body. A constant force coefficient is not sufficient to predict forces for all flow conditions. For example, aerodynamic force coefficients may be a function of Mach number and Reynolds number ($Re$). If the relevant forces are a weak function of these parameters, using an off-condition coefficient (slightly different geometry, different size, etc.) can still give a reasonable prediction of force magnitudes.

The blade-element method is simply the application of 2.18 to chord-wise strips along a flapping wing. Figure 2.1 shows a sample wing strip. The wing must be divided into strips because the local velocity varies along the wing. For the decidedly subsonic insect flapping regime, force coefficients should vary with $\alpha$, $Re$, and wing shape. Ideally, these variations will be clear trends that experiments can identify. If force (or moment) coefficients begin to vary with the details of the flapping kinematics, or if they depend on products of these changes, the usefulness of the blade-element method is severely reduced.

The blade-element method estimates forces based only on instantaneous flow conditions, making the method *quasi-static*. Unsteady flow features, such as wake capture, cannot be directly modelled. They may enter indirectly, for example, if the force coefficient is a function of $\alpha$, and the time-dependent force appears periodically, with the time of occurrence corresponding to a particular $\alpha$. However, if the flapping motion becomes aperiodic, such as during a maneuver, or if the periodic flapping kinematics are changed significantly, then the previously-tailored $\alpha$-dependence will produce erroneous results.

**Aerodynamic forces**

In hover, the ambient air velocity is negligible, so the dynamic pressure on the wing develops only through its relative motion. Thus, the aerodynamic force components on each chord-wise strip can be expressed as

$$\mathrm{d}F_{aero} = \underbrace{\frac{1}{2}\rho\omega_h^2\left(r' + x_r\right)^2}_{q} \underbrace{C_F(\alpha)}_{C_F} \underbrace{c(r')\mathrm{d}r'}_{\mathrm{d}S}, \tag{2.19}$$

which is simply a rearranged form of 2.18. When there is no stroke plane deviation, $\omega_h = -\dot{\phi}$.

The total aerodynamic force is commonly decomposed into lift and drag components, $F_L$ and $F_D$. Drag is directed in opposition to the relative ambient velocity, and lift, orthogonal. Experiments and CFD calculations [11, 2] have shown consistent functional forms for the variation of lift and drag coefficients with $\alpha$,

$$\begin{aligned} C_L(\alpha) &= C_{L_{max}} \sin(2\alpha), \\ C_D(\alpha) &= \left(\frac{C_{D_{max}} + C_{D_0}}{2}\right) - \left(\frac{C_{D_{max}} - C_{D_0}}{2}\right) \cos(2\alpha). \end{aligned} \tag{2.20}$$

For the Reynolds number ($\approx 100$), geometry, and flapping kinematics of a typical *Drosophila* wing, [11] found by experiments that these coefficient forms are best fit by

$$\begin{aligned} C_{L_{max}} &= 1.8 \\ C_{D_0} &= 0.4 \\ C_{D_{max}} &= 3.4 \end{aligned} \tag{2.21}$$

These values are a common starting point for blade-element force estimates. Experiments or CFD simulations are used to refine them for specific wing shapes and Reynolds numbers.

Integrating 2.19 for the lift component leads to

$$F_L = \frac{1}{2}\rho\omega_h^2 C_L(\alpha)\bar{c}R^3 \underbrace{\int_0^1 (\hat{r} + \hat{x}_r)^2 \hat{c}(\hat{r})\mathrm{d}\hat{r}}_{\equiv \hat{F}} \tag{2.22}$$

where $\hat{F}$ is the non-dimensional aerodynamic force. The integral is easily performed

to yield

$$\hat{F} = \hat{r}_2^2 + 2\hat{x}_r\hat{r}_1 + \hat{x}_r^2. \tag{2.23}$$

If $\hat{x}_r$ is zero (which can always be arranged), then the non-dimensional aerodynamic force is simply equal to $\hat{r}_2^2$. The drag force has an identical expression, the only difference being the coefficient. The unit vectors for lift, drag, and the normal component of the aerodynamic force are defined as

$$\begin{aligned} \boldsymbol{e}_L &= -\boldsymbol{e}_{\omega_h} \\ \boldsymbol{e}_D &= -\boldsymbol{e}_{v_h} \\ \boldsymbol{e}_N &= -\operatorname{sgn}(\alpha)\,\boldsymbol{e}_z. \end{aligned} \tag{2.24}$$

These definitions take into account the chosen sign convention for $\alpha$, and the sign conventions of $C_L$ and $C_D$, as used in 2.20. The normal force coefficient is found by a simple rotation, $C_N = \cos(\alpha)C_L + \sin(\alpha)C_D$.

**Rotational-axis aerodynamic moment**

The aerodynamic moment about the axis of rotation ($x$-axis) is more complicated because the chord-wise position of the center of pressure depends on the instantaneous angle-of-attack and on the detailed shape of the leading edge. The required integral is

$$M_{x,aero} = \frac{1}{2}\rho\omega_h^2 C_N(\alpha)\int_0^R y_{cp}(r')\,(r' + x_r)^2\,c(r')\mathrm{d}r', \tag{2.25}$$

where $y_{cp}(r')$ is the distance from the hinge line to the center of pressure. Dickson [12] reports experimental data on the location of the center of pressure as a function of

$\alpha$, for *Drosophila*,

$$\hat{d}_{cp} = \frac{0.82}{\pi}|\alpha| + 0.05, \tag{2.26}$$

where $\alpha$ is in radians, and $\hat{d}_{cp}$ is the non-dimensional location of the center of pressure, measured back from the leading edge (i.e. 0 for the leading edge and 1 for the trailing edge). In the $xy$-frame, the location of the center of pressure for each strip is

$$y_{cp} = y_r + y_{LE}(r') - c(r')\hat{d}_{cp}. \tag{2.27}$$

Inserting into 2.25 yields

$$M_{x,aero} = \frac{1}{2}\rho\omega_h^2 C_N(\alpha)\bar{c}^2 R^3 \int_0^1 \left[\hat{y}_r + \hat{y}_{LE}(\hat{r}) - \hat{c}(\hat{r})\hat{d}_{cp}(\alpha)\right](\hat{r} + \hat{x}_r)^2\,\hat{c}(\hat{r})\mathrm{d}\hat{r}. \tag{2.28}$$

Thus the location of the net center of pressure is

$$\hat{Y}_{cp} = \frac{\int_0^1 \left[\hat{y}_r + \hat{y}_{LE}(\hat{r}) - \hat{c}(\hat{r})\hat{d}_{cp}(\alpha)\right](\hat{r} + \hat{x}_r)^2\,\hat{c}(\hat{r})\mathrm{d}\hat{r}}{\hat{F}}, \tag{2.29}$$

with the resulting rotational moment expression

$$\boldsymbol{M}_{x,aero} = -\operatorname{sgn}(\alpha)\frac{1}{2}\rho\omega_h^2 C_N(\alpha)\bar{c}^2 R^3 \hat{F}\hat{Y}_{cp}(\alpha)\boldsymbol{e}_x. \tag{2.30}$$

Calculating and measuring aerodynamic moments is notoriously more difficult than aerodynamic forces. The root of this problem is that moments are highly sensitive to changes in the location of the center of pressure. For an insect wing, the distance between the torsional axis and center of pressure may only be 10% of the mean chord, so even small changes in position have a large effect on the resulting moment.

### Rotational aerodynamic forces

The aerodynamic force previously described, sometimes called the "translational" aerodynamic force, is not a function of the instantaneous rotation rate. The influence of rotation is felt only indirectly through the $\alpha$-dependence of the force coefficients. There is evidence [39] that independent "rotational" forces exist, which *are* a function of the instantaneous rotation rate.

The original adopted model for these forces is that of a thin wing fluttering at low $\alpha$, with the rotational forces arising from a coupling of translation and rotation. This force has the form

$$\mathrm{d}F_{rot} = \frac{1}{2}\rho\omega_x\omega_h c(r' + x_r)C_R(\alpha)c(r')\mathrm{d}r'. \tag{2.31}$$

Experiments [39] have shown that $C_R$ varies both with rotation rate ($\omega_x$) and the location of the rotational axis ($\hat{y}_r$). This force is not included in any calculations presented here, primarily because improved predictions of lift force could not be realized, and contributions to rotational moment could not be measured. Future experimental investigations, should they investigate this force, especially for the purposes of passive rotation, must include direct measurements of rotational moments to calculate the center of pressure of these rotational forces.

### Aerodynamic damping

The aerodynamic forces and moments discussed so far provide limited rotational damping to the system. Passive rotation experiments (v.i. section 2.3.3) confirmed that without such a term, the predicted wing trajectories are severely under-damped. In addition, consider the pathological case of a wing rotating, but not flapping.

Clearly there will be aerodynamic moments exerted on the wing, though the translational and rotational aerodynamic force terms (equations 2.22 and 2.31) would predict none.

For this term, the relative velocity due only to rotation of the wing is considered. The relative air velocity is zero at the hinge axis and increases linearly away from it, as illustrated in figure 2.5. Using a dynamic pressure based on this velocity, it is straightforward to adapt 2.19 to form the rotational damping moment for a differential element as

$$\mathrm{d}(\delta M_{rd}) = -\frac{1}{2}\rho(\omega_x y)^2 C_{rd}|y|\mathrm{d}r'\mathrm{d}y, \tag{2.32}$$

where each chordwise strip is further divided, as in figure 2.1, into differential elements of height d$y$ which are located a distance $y$ from the hinge axis. Integrating with respect to $y$ yields $\delta M_{rd}$, the damping moment contribution from a single chordwise strip:

$$\begin{aligned} \delta M_{rd} &= -\frac{1}{2}\rho\omega_x^2 C_{rd}\mathrm{d}r' \int_{y_0}^{y_1} |y|y^2\mathrm{d}y & (2.33)\\ &= -\frac{1}{2}\rho\omega_x^2 C_{rd}\mathrm{d}r' \left(\frac{1}{4}|y_1|y_1^3 - \frac{1}{4}|y_0|y_0^3\right), & (2.34) \end{aligned}$$

where

$$\begin{aligned} y_0 &= y_r + y_{LE}(r) - c(r) \quad \text{and} \\ y_1 &= y_r + y_{LE}(r) & (2.35) \end{aligned}$$

are the coordinates of the trailing and leading edges of the wing. Switching to non-dimensional coordinates results in

$$\delta M_{rd} = -\frac{1}{2}\rho\omega_x^2 C_{rd}\bar{c}^4 R\hat{y}_{rd}(\hat{r})\mathrm{d}\hat{r}, \tag{2.36}$$

where

$$\hat{y}_{rd}(\hat{r}) = \frac{1}{4}\left[|\hat{y}_r + \hat{y}_{LE}|(\hat{y}_r + \hat{y}_{LE})^3 - |\hat{y}_r + \hat{y}_{LE} - \hat{c}|(\hat{y}_r + \hat{y}_{LE} - \hat{c})^3\right] \tag{2.37}$$

is the non-dimensional location of the effective moment arm of the rotational damping term for a single wing strip. Integrating these chordwise strips results in the total damping moment for the wing,

$$\boldsymbol{M}_{x,rd} = -\frac{1}{2}\rho\omega_x|\omega_x|C_{rd}\bar{c}^4 R\hat{Y}_{rd}\boldsymbol{e}_x, \tag{2.38}$$

where

$$\hat{Y}_{rd} = \int_0^1 \hat{y}_{rd}(\hat{r})\mathrm{d}\hat{r}. \tag{2.39}$$

This approach was also used [2] in experiments with tumbling cards, using a rotational damping moment coefficient $C_{rd} = 2.0$, likely because this is the classical result for the two-dimensional drag coefficient of a flat plate normal to a uniform flow. As the rotationally-induced velocity is normal to the wing, it would be natural, in the present case, to use $C_{D_{max}}$. For all calculations in this work, a value of 5.0 was used. This value, in general, led to the best agreement between measured and predicted passive rotation trajectories. However, the predictions were not highly sensitive to the exact value. Values of $C_{rd}$ in the 3–6 range all showed good agreement. The main challenge in determining this term to higher precision is the difficulty in separating errors in the value of $C_{rd}$ from errors in the location of the center of pressure. Experiments that explicitly measure the moment about the rotational axis are likely required to better clarify the magnitude and variation of this parameter.

If the rotational axis does not pass through the chord center, a net force will also result. For all calculations in this paper, these forces were neglected. The main reason

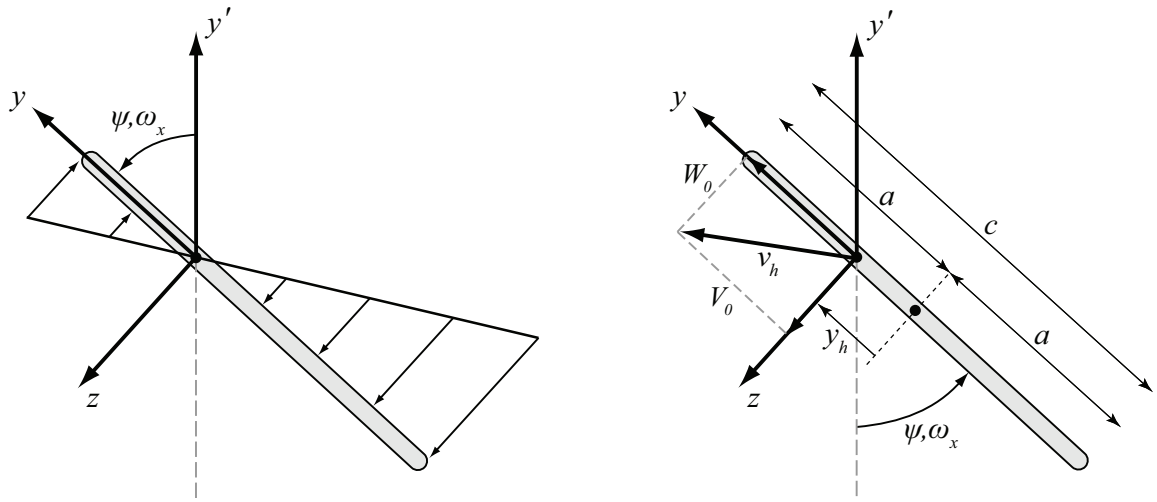


Figure 2.5: The left image shows a wing segment in pure rotation, and the resulting relative velocity profile seen by the wing. The right image shows the pertinent dimensions and variables for calculating the added mass forces and moments.

is one of complexity. It is easy to quickly amass several coefficients which may be "tuned" for a specific experimental result. It would be difficult to decide what is a result of pure rotational damping, and what is a result of a flapping–rotation coupled "rotational" aerodynamic force.

### Added mass effects

The concept of "added mass" (or "virtual" mass) is best understood as the aerodynamic forces and moments that are dependent upon a body's acceleration, be it translational or rotational. In the strictest sense, added mass forces and moments are only those that result from the solution of the Euler equations without circulation (potential flow). Aerodynamic forces and moments dependent upon acceleration may also occur as a result of viscous effects, a notable example being the Basset force [54], which represents forces that occur due to an acceleration-dependent lag in boundary

layer development, though all viscous-based acceleration forces are sometimes called Basset forces. Without strong evidence of their importance and an accurate method to predict them, Basset forces will not be accounted for separately. Their influence, if any, will find its way into the standard aerodynamic force and moment coefficients, which are derived from experiments.

There is no analytical solution to the potential flow equations for a general two dimensional wing planform moving in a three dimensional fashion. However, the potential flow solution for an arbitrary two dimensional body translating and rotating in two dimensions is well known. Application of this solution easily gives the added mass forces and moments for a thin wing section. From [40],

$$\begin{aligned} Z_0 &= -\lambda_z \dot{W}_0 - \lambda_{zy}\dot{V}_0 - \lambda_{z\omega}\dot{\omega}_x - \omega_x\left(\lambda_{zy}W_0 + \lambda_y V_0 - \lambda_{y\omega}\omega_x\right) \\ Y_0 &= -\lambda_{zy}\dot{W}_0 - \lambda_y \dot{V}_0 - \lambda_{y\omega}\dot{\omega}_x + \omega_x\left(\lambda_z W_0 + \lambda_{zy}V_0 + \lambda_{z\omega}\omega_x\right) \\ \mathfrak{M}_0 &= -\Big[\lambda_{z\omega}\dot{W}_0 + \lambda_{y\omega}\dot{V}_0 + \lambda_\omega\dot{\omega}_x + \lambda_{zy}(V_0^2 - W_0^2) \\ &\qquad + (\lambda_z - \lambda_y)W_0V_0 + \omega_x(\lambda_{z\omega}V_0 - \lambda_{y\omega}W_0)\Big], \end{aligned} \tag{2.40}$$

where $Z_0$ and $Y_0$ are the added mass forces (per unit depth) in the $z$- and $y$-directions, and $\mathfrak{M}_0$ is the added mass moment per unit depth. $W_0$ and $V_0$ are the components of the velocity of the wing at its axis of rotation (see figure 2.5). The $\lambda_{ab}$ terms are the "coefficients of added mass". Repeated subscripts are dropped. The wing section shown in figure 2.5 has effectively zero thickness and a rotational axis offset from the midpoint by $y_h$, which can be expressed non-dimensionally as

$$\hat{y}_h(\hat{r}) = \frac{1}{2}\hat{c}(\hat{r}) - \hat{y}_{LE}(\hat{r}) - \hat{y}_r. \tag{2.41}$$

The non-zero added mass coefficients for a thin flat wing section are

$$\begin{aligned} \lambda_z &= \pi\rho a^2 \\ \lambda_{z\omega} &= -\pi\rho a^2 y_h \\ \lambda_\omega &= \pi\rho a^2 y_h^2 + \frac{1}{8}\pi\rho a^4, \end{aligned} \tag{2.42}$$

where $a$ is the semi-chord and $\rho$ is the density of the surrounding air. Notice that many of the terms in 2.40 are "cross-term" accelerations and not pure rotations. These will not be considered, as they will duplicate existing blade-element terms with similar forms, such as the rotational force and damping terms. The validity of these terms (as well as the pure acceleration terms) is already in question, as this formulation assumes fully attached irrotational flow in two dimensions. After eliminating cross-terms and terms with zero-valued coefficients, 2.40 is reduced to

$$\begin{aligned} Z_0 &= -\lambda_z \dot{W}_0 - \lambda_{z\omega}\dot{\omega}_x \\ Y_0 &= 0 \\ \mathfrak{M}_0 &= -\lambda_{z\omega}\dot{W}_0 - \lambda_\omega \dot{\omega}_x. \end{aligned} \tag{2.43}$$

The normal acceleration is given by $\dot{W}_0 = -r(\dot{\omega}_y - \omega_x\omega_z)$. Substitution and radial integration yields

$$M_{x,am} = -\left(\frac{\pi}{4}\rho\bar{c}^3 R^2 \hat{I}_{xy,am}\right)(\dot{\omega}_y - \omega_x\omega_z) - \left(\frac{\pi}{4}\rho\bar{c}^4 R\hat{I}_{xx,am}\right)\dot{\omega}_x \tag{2.44}$$

where

$$\begin{aligned} \hat{I}_{xy,am} &= \int_0^1 (\hat{r} + \hat{x}_r)\hat{c}(\hat{r})^2 \hat{y}_h(\hat{r}) \mathrm{d}\hat{r} \\ \hat{I}_{xx,am} &= \int_0^1 \hat{c}(\hat{r})^2 \left(\hat{y}_h(\hat{r})^2 + \frac{1}{32}\hat{c}(\hat{r})^2\right) \mathrm{d}\hat{r}. \end{aligned} \tag{2.45}$$

A similar integration yields the added mass term, $F_{z,am}$.

## 2.3 Passive rotation experiments and analysis

Using the blade-element method to estimate aerodynamic torques raises two major concerns. The first is whether the quasi-steady approximation is overly limiting. Wake capture effects and other path-dependent phenomena must be negligible. The second concern is the validity of force and moment coefficients. The method is useless if different force and moment coefficients are required for every operating condition and wing shape. More precisely, aerodynamic coefficients must change little for reasonable changes in flapping frequency, flapping kinematics, and wing shape. Quantification of "little" and "reasonable" is arbitrary.

Experiments are needed to assess the performance of the blade-element method in predicting time-dependent forces and moments. If wing kinematics and forces are measured simultaneously, force coefficients for each wing and kinematics configuration can be extracted. If the experiments are done with passively rotating wings, the validity of 2.15 can be directly assessed.

### 2.3.1 Experimental setup and calibration

A testing setup, illustrated in figure 2.6, was constructed for the synchronized measurement of three degree-of-freedom flapping kinematics ($\phi(t)$, $\theta(t)$, $\psi(t)$) and lift forces on robotically-driven wings. Although all wings tested here are of artificial construction, the setup does not preclude the use of natural wings. Kinematics are determined a posteriori using stereoscopic reconstruction of high-speed video recordings.

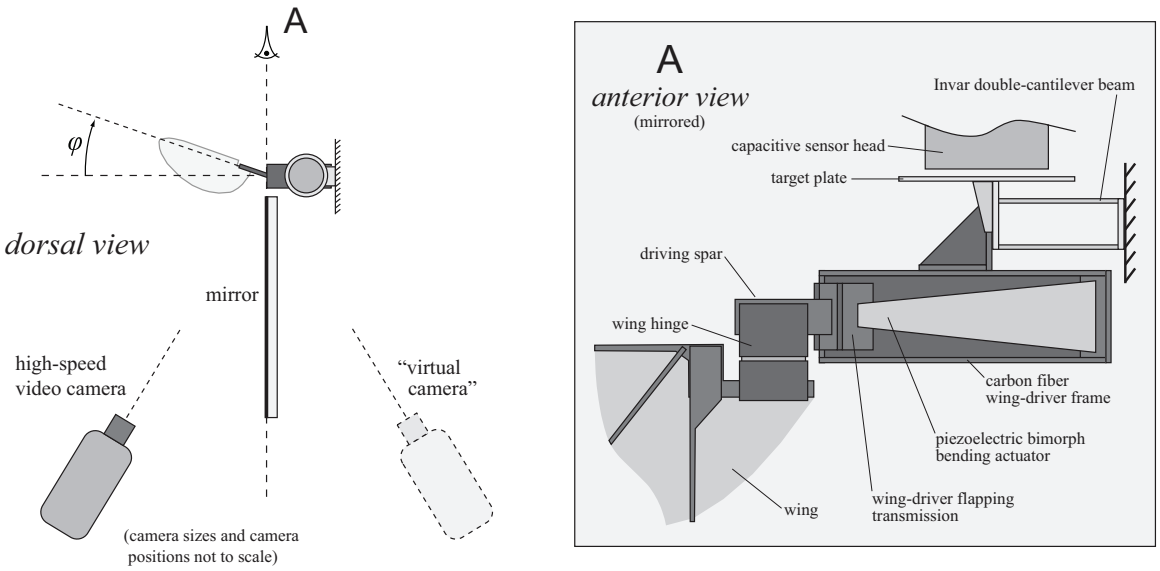


Figure 2.6: Diagram of experimental setup for measuring lift forces and capturing wing motion using high-speed video. The wing-driver is attached to an Invar double-cantilever beam. The beam deflection is measured by a capacitive displacement sensor. A mirror generates a second camera view, allowing stereoscopic reconstruction.

The wing driver mechanism is mounted on the end of a double-cantilever beam. The beam's deflection is measured with a capacitive displacement sensor. To my knowledge, these are the first reported experiments that measure three degree-of-freedom flapping kinematics, synchronized to real-time force measurements, for insect-scale flapping wings.

The wing is flapped using a piezoelectric bimorph actuator, of the type described by [51], mounted in a carbon fiber frame. The linear displacement of the drive actuator is mapped to an angular flapping motion using a transmission mechanism of the type described by [49]. The actuator is made as small as possible to minimize the effective mass of the beam–driver system, thus maximizing sensor bandwidth.

The double-cantilever beam is laser-cut and folded from 150$\mu$m sheet Invar [52]. Abutting folded edges are soldered or laser-welded together. The double-cantilever

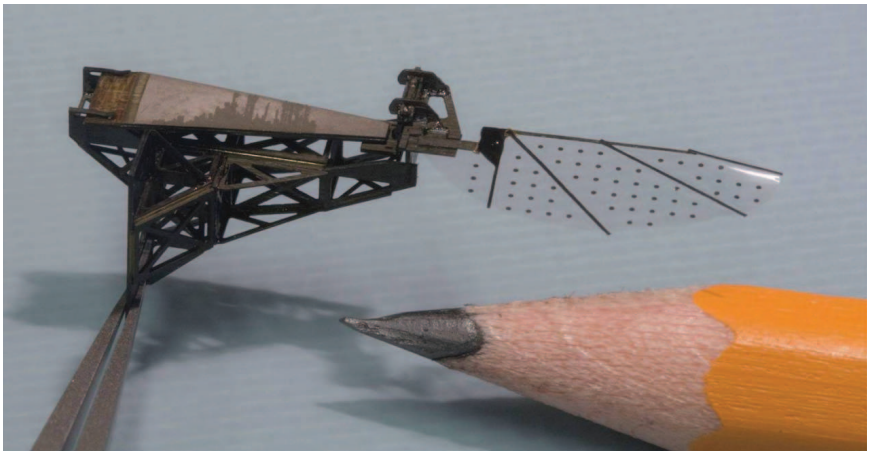

Figure 2.7: The one-wing flapping mechanism and attached wing are manufactured using the same methods used to make flight-worthy flapping wing MAVs.

topology ensures that the beam deflects linearly without rotation. The dual beams are 7mm long, 4mm wide, and spaced vertically by 3mm. The 10mm diameter capacitive sensor target plate, also laser-cut from Invar sheet, is attached to the end of the beam with a pair of triangular support ribs. These ribs also serve to stiffen the end-plate of the beam to maintain the desired built-in boundary condition. The mass of the wing driver (frame, actuator, transmission) is approximately 150mg. Using simple beam theory, the predicted sensor resonant frequency is 950Hz. This includes the effect of wing driver mass, target plate and support rib mass, and the theoretical effective mass of the sensor beam. The measured resonant frequency of the system, determined by impulse testing, is 810Hz. All reported force data has been post-processed with a high-order zero-phase 750Hz digital low-pass filter. The force sensor was calibrated using multi-point static loading with known masses. No attempts at dynamic calibration (cf. [22]) have been made. Sensor output is 1.04mg/mV, with a measured noise floor of 1.5mV, at full bandwidth. All force data is reported as

mass-equivalent using a gravity acceleration of $9.8\text{m/s}^2$.

A high-speed video camera is used to record wing motion. All video recordings were captured at $10,000$ frames per second, with exposure times of $30\mu$s. As shown in figure 2.6, a mirror provides a second camera view. The camera points toward the wing from approximately $\phi = -60°$. The camera is positioned at least 150mm away from the wing (10 wing lengths) to minimize aerodynamic disturbance. The primary view and virtual camera view are illuminated by backlight; fiber-optic light guides direct light from standard tungsten halogen illuminators onto diffusion screens, each positioned 150mm behind the wing. The ground plane (optical table) is located 200mm below the wing.

A computer with a real-time control board sends drive signals to high-voltage amplifiers, which drive the piezoelectric actuator. The same board issues camera trigger signals and samples the capacitive displacement sensor at 5kHz. Synchronization between the trigger signal and the camera frame buffer was confirmed by recording a light-emitting diode being driven directly by the trigger signal. Synchronization between video frames and the force signal was confirmed by recording an impulse impact on the driving spar and matching the time-of-impact video frame with the force signal.

### 2.3.2 Extracting flapping kinematics

Stereoscopic calibration of the camera setup is accomplished using the methods of [56] and [8]. Several images of a checkerboard with known dimensions are taken. The checkerboard is placed at several positions and with several orientations to the

camera, with care that the complete pattern is seen by both the real and virtual camera. The images are used to fit a lens distortion model and the relative positioning between the two cameras is calculated. The resulting calibration maps row-column pixel coordinates for the real and virtual images (corresponding to the same physical point) to a three-dimensional location relative to the real camera.

Three points are tracked on the wing, with their coordinates used to define an instantaneous mean wing plane for each video frame. Figure 2.3 shows a photograph of the wing used for all experiments presented here. The first, second, and fourth (proximal to distal) spar ends are used for the tracking points. A normal vector defined by these points is projected onto fixed axes to extract the flapping, out-of-plane, and rotational angles. Figure 2.8 shows a sample frame from a captured video recording. For all experiments carried out, the wing stayed very flat, and did not deviate very far from the rigid body ideal. Figure 2.9 shows a frame sequence which is characteristic of the maximal amount of wing fluttering and spar bending observed. While in these experiments the intent was to suppress wing deformations, these tracking techniques could easily be used to reconstruct higher-order oscillation and deflection modes by tracking more points.

Each video recording consists of two full flapping periods. The hinge line (torsional axis) is determined from an image of the wing at rest; it is identified as the midline of the wing hinge flexure. The position and orientation of the hinge line in then determined by offset in local coordinates for each frame in the flapping sequence. A plane is fit through the track left by the hinge line, over the full time sequence, to define the so-called mean stroke plane, which establishes a reference for defining

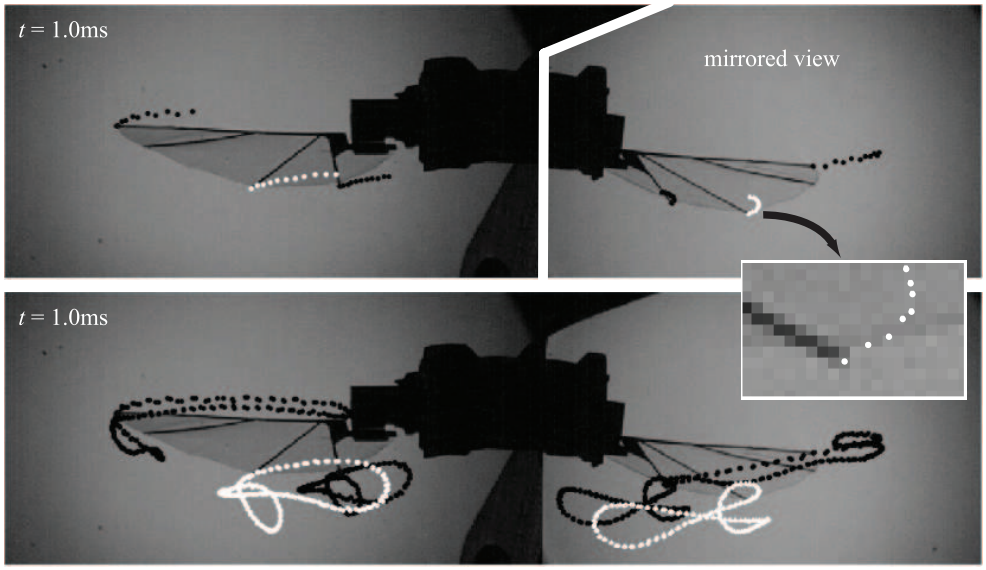


Figure 2.8: The 11th frame of the baseline 100Hz case is shown in both images. The top image highlights the mirror edge and labels the real and virtual images, and shows tracked spar endpoints for the first 11 frames. The bottom image shows tracking results from a complete 200-frame, 2-period sequence. The high degree of periodicity is evident from the pair-wise clustering of the points. The spar ends are tracked manually, for each frame, on a sub-pixel basis.

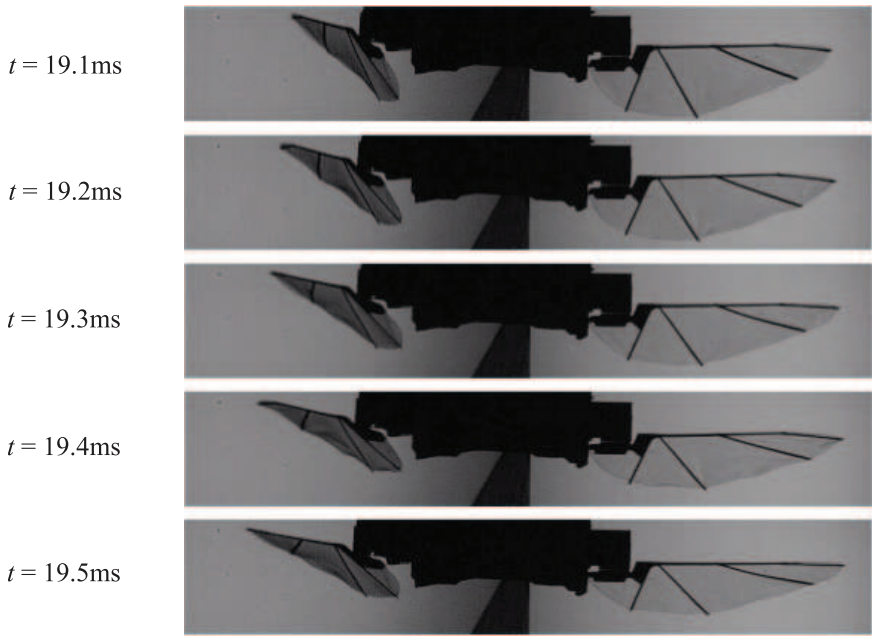


Figure 2.9: This sequence, taken from the 100Hz baseline case, shows observed membrane fluttering and spar bending. The two most distal spars are clearly seen to flex between the fourth and fifth frames.

out-of-plane motion, $\theta(t)$. The wing orientation calculated from an image of the wing at rest is used to define the flapping angle origin, ($\phi = 0$). A sphere is fit to the point cloud left by the track of the distal edge of the wing hinge to determine the radial offset of the wing from the center of rotation.

All plots of measured angular trajectories are shown unfiltered, in degrees. However, when derivatives are calculated for use by the blade-element method, filtering is applied to prevent excessive noise.

### 2.3.3 Experimental results

The following experiments all use the same wing design. The two experiments flapping at 100Hz use the same "short" wing hinge, and the 70Hz case uses the

"long" hinge.

The measured values of $\psi$ and $\dot{\psi}$ at $t = 0$ provide the initial condition. All calculations to predict the rotational trajectory of the wing are made by integration of equation 2.15. This means that measurements of out-of-plane deviation, $\theta(t)$, contribute to the solution. However, all experiments presented here do not contain significant out-of-plane motion, as the flapping mechanism does not support it. In practice, trajectories predicted by 2.16 are very similar. The small amount of out-of-plane deviation that does occur is a result of wing hinge compliance. While designed to be much more compliant in the rotational axis, the off-axis compliance is enough to allow a few degrees out-of-plane motion when under high load.

Lift coefficient, $C_{L_{max}} = 1.7$, is used for *all* calculations. This value provides good general agreement with all experiments performed, and is very close to 1.8, the classic *Drosophila* value. Drag data from [11], and the $\hat{d}_{cp}(\alpha)$ trend reported by [12], given in equation 2.26 is used, as none of the current experiments directly measure these values. The same rotational damping coefficient ($C_{rd} = 5.0$) was used for all calculations. Unless otherwise noted, no rotational aerodynamic forces or rotational added inertia terms were applied (though the added mass lift *force* is included).

In the following plots, unless otherwise noted, the term "lift" indicates the reaction force of the wing on the drive spar, i.e.

$$F_N = F_{aero,X'} - m\, a_{X'}, \tag{2.46}$$

where $F_N$ is the total lift, $F_{aero,X'}$ is the projection of the total aerodynamic force vector onto the $X'$-axis, $m$ is the wing mass, and $a_{X'}$ is the linear acceleration of the center of mass of the wing. It is important to note that "lift" in the current sense

is different than "lift" in the sense of the blade-element method. The unit vector $\boldsymbol{e}_L$ used in blade-element calculations always points normal to the *instantaneous* stroke plane, rather than the *mean* stroke plane, which is the plane of reference for $F_N$ and $F_{aero,X'}$.

All measured *mean* lift values are obtained by averaging over 10 periods, while the calculated lift values are derived from the kinematics captured during the first two of those periods. The inertial component has zero mean when the wing motion is perfectly periodic, but the instantaneous values of the inertial contribution are non-trivial, and must be added to aerodynamic lift predictions when comparing to experimental measurements.

In general, working at-scale poses the extra challenge of dealing with wing inertial forces, which are typically of the same order as the aerodynamic forces. Subtracting them out requires high quality kinematics measurements to extract the crucial angular accelerations. Measuring wing mass with an electrobalance is easy, but measuring inertias and products of inertia is not trivial. The $I_{xx}$ and $I_{xy}$ values used here were calculated from a three dimensional computer model of the wing, using measured material densities. The wing center of mass was also calculated from this model. As a check, measured masses were confirmed to agree with predicted masses from the model.

The hinge stiffness is simply calculated using equation 2.12, using the hinge geometry parameters and the specification-sheet modulus for the polyimide film used to make the hinge flexure. Potential hinge stiffness non-linearity and damping have not been characterised.

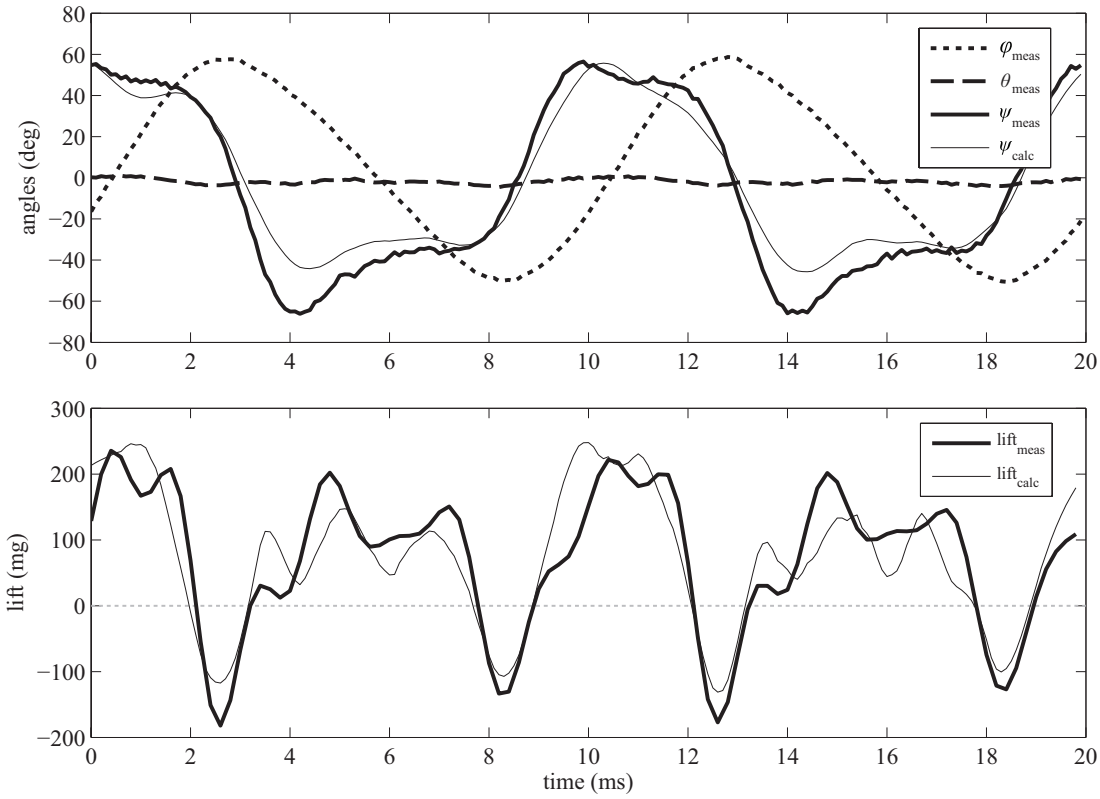


Figure 2.10: Baseline 100Hz flapping case (short hinge). Measured kinematics are plotted unfiltered. Predicted wing rotation does not include any rotational aerodynamic force or rotational added inertia terms. Predicted lift includes inertial reaction of the wing and theoretical added mass lift.

### Baseline 100Hz flapping experiment

The first case (the "baseline") examines passive rotation at 100Hz. The flapping amplitude, $\Phi$, is 108°. Figure 2.10 plots the measured kinematics and predicted rotation in the top graph. The out-of-plane motion is only a few degrees. The transmission mechanism is not perfectly symmetric, and real-time position feedback is not currently available. The downstroke experiences larger lift forces, as the wing velocity is slightly higher then. The mean measured lift is 71.6mg, and the calculated lift is 73.7mg.

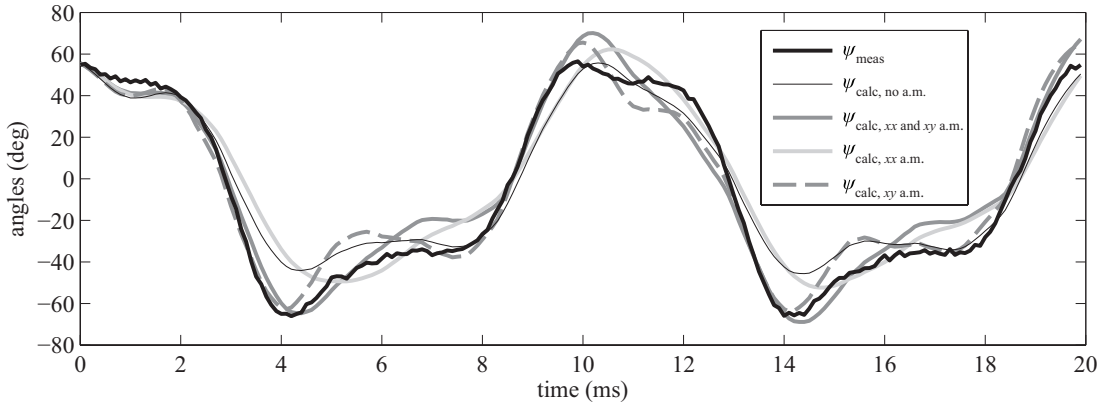


Figure 2.11: Baseline 100Hz flapping case (short hinge). Measured wing rotation and predicted wing rotation using each combination of the theoretical rotational added inertia terms.

Figure 2.11 shows predicted rotation, for the same case, with different combinations of the $I_{xx,am}$ and $I_{xy,am}$ terms. It appears that inclusion of the $I_{xy,am}$ term improves the prediction of the maximum amount of negative rotation, but the agreement is compromised in other areas. These differences were investigated in other experimental data sets, and no consistent improvement for any of these added inertia terms could be found. This does not mean that they are not important, but their contribution is simply less than the uncertainty introduced by other factors, such as center of pressure location and non-linear hinge compliance.

Figure 2.12 shows each component of the predicted lift force. It is clear that subtracting the inertial contribution is critical for analyzing the aerodynamic contribution. At end of a stroke, when the wing flips, wing velocity, and thus lift, is low, while vertical acceleration of the center of mass is high (centripetal acceleration), leading to an inertial reaction peak (negative lift peak). This effect is more or less relevant depending on the mass of the wing, rate of flip, and other factors.

From Figure 2.13, it is clear that an additional rotational aerodynamic damping

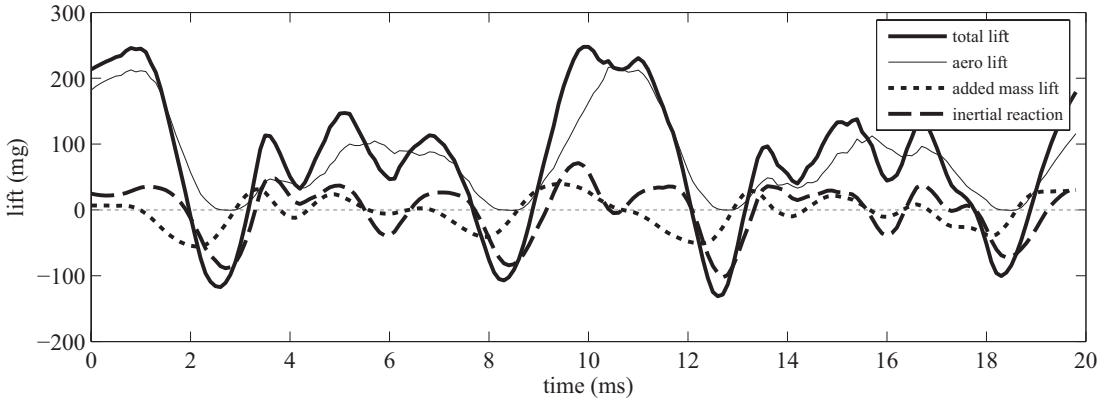


Figure 2.12: Baseline 100Hz flapping case (short hinge). The predicted total lift force is broken down into constituent components.

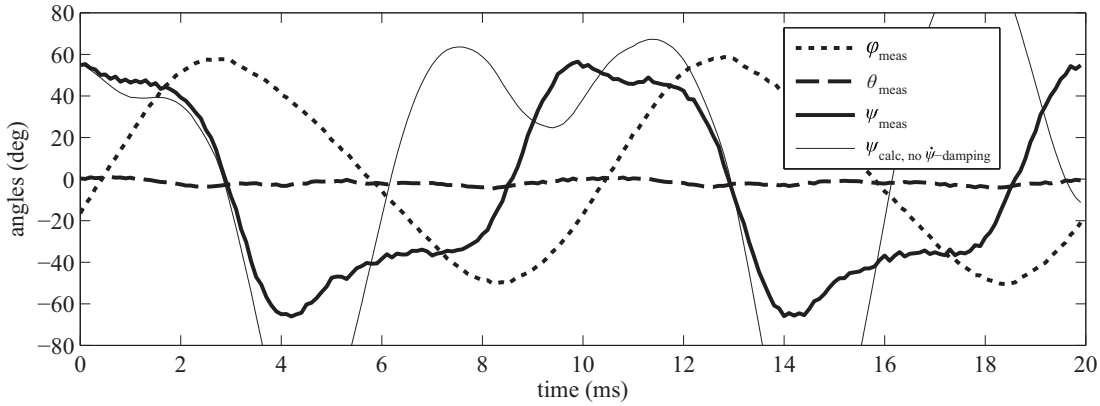


Figure 2.13: Baseline 100Hz flapping case (short hinge). Measured (all) and predicted (rotational only) kinematics are again plotted, except the prediction does not include a pure rotational damping term.

term is critical to the prediction of realistic rotational dynamics. As mentioned earlier, refinement of this component will require experiments that can directly measure rotational torques.

### Split-cycle flapping experiment

The next experiment presented uses the same wing, with the same wing hinge, flapping at the same fundamental frequency. However, the full flapping period is a

concatenation of a longer duration upstroke and a shorter duration downstroke. The upstroke-to-downstroke duration ratio, called $\tau_{ss}$, is 0.62 in this case. The asymmetry in $\phi(t)$ is readily apparent in figure 2.14. This type of flapping is called "split-cycle", which is aimed at breaking the upstroke-downstroke symmetry to create net (roll) moments about the vertical axis. This technique [13] was proposed as a method to control roll for a flapping-wing robotic insect without needing a separate actuator to control $\psi$ independently. For this case, the measured lift is 71.2mg, almost identical to the baseline case. The predicted lift, using the same lift coefficient as the baseline case, is 75.7mg. Since roll torques were not measured, the effectiveness in generating a net moment cannot be assessed, but it is clear that the rotational kinematics can be made very asymmetric without changes in mean lift, while operating under the restrictions of a passively rotating system.

Agreement between the predicted and measured lift forces, on a time-varying as well as mean value basis, is excellent, even though the peak lift force in the split-cycle case is almost twice that of the baseline case. The blade-element method, in this case, is highly tolerant of drastic changes in flapping and rotational kinematics. In spite of the uncertainties in drag coefficients, center of pressure location, damping, and rotational forces, the approximate values based on published data for *Drosophila* lead to good predictions of passive rotation dynamics.

**70Hz flapping experiment**

For the final experiment, the wing hinge was lengthened, allowing the wing to achieve sufficient rotation when flapped at 70Hz. The total flapping angle is also

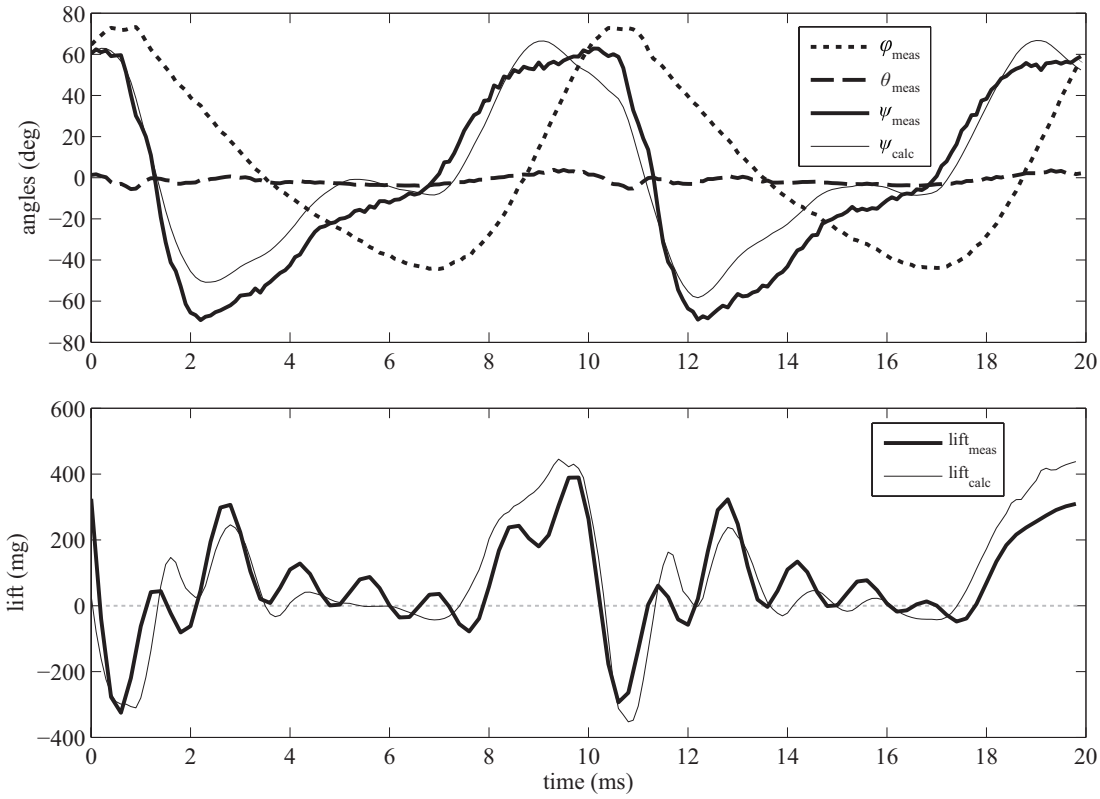


Figure 2.14: 100Hz flapping case (short hinge), now with $\tau_{ss} = 0.62$ split-cycle flapping angle kinematics.

reduced to 90°. The measured lift is 30.4mg, and the predicted lift is 26.6mg (same coefficients as all other cases). Trajectory and force results are plotted in figure 2.15. There appears to be a small phase discrepancy between the measured and predicted rotation angle, while the amplitude prediction is excellent. On the other hand, the baseline case showed excellent phase agreement, with small disagreements at times in amplitude. The various model uncertainties are not small enough to draw general conclusions on the sources of these discrepancies. It is possible that wake capture effects and rotational aerodynamic effects are contributing to the observed forces, but, at this time, the data available is not fine enough to separate these effects from other aerodynamic uncertainties. It is clear, at least for the range of cases examined here, that exclusion of these effects does not preclude accurate estimates of wing passive rotation trajectories.

## 2.4 Discussion

In these experiments, the predicted and measured lift forces show excellent agreement, both in mean value and detailed time-history. These predictions were consistent across large changes in flapping kinematics, flapping frequency, and flapping amplitude, without any changes to model coefficients. These experiments reveal that coping with inertial wing forces is an important challenge when working with actual-size wings. Minimizing the influence of these inertial forces in isolating aerodynamic loads will be critical for continued success in at-scale studies of flapping wing aerodynamics. It is difficult to quantify the agreement of measured kinematics with passive rotation predictions. Qualitatively, the rotational dynamics were well captured, in-

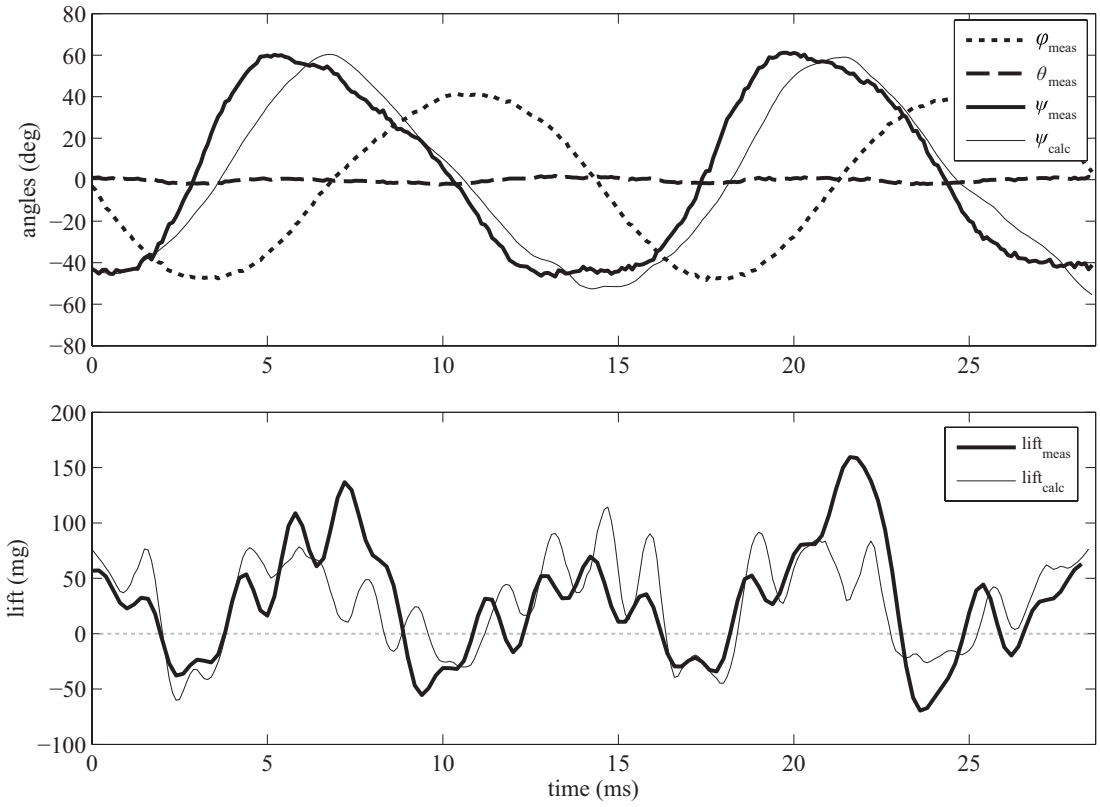


Figure 2.15: 70Hz flapping case (long hinge). A longer hinge (more hinge compliance) allows an appropriate amount of wing rotation when flapping at a lower frequency.

cluding sub-period modes. Quantitatively, peak rotational amplitudes, rates, and phases showed good agreement with measured values. Demonstration of asymmetric split-cycle kinematics, without reductions in lift force, strongly motivate further investigation of this wing control strategy.

Improvements in passive rotation trajectory predictions will not come without a great deal of work in measuring and characterising flight forces and moments. Rotational moments in particular must be measured for a variety of wing shapes, sizes, and flapping profiles. In spite of this lack of data, the blade-element method, when used with published data, provides very good predictions of passive rotation trajectories. It is eminently useful in the design of robotic wing hinges. These methods can now be used, with confidence, to study achievable optimal kinematics under the reduced input control available with a passive rotation system.

These experiments lay the groundwork for exciting future studies of natural insect wings, and artificial wings that include distributed compliance. This work has demonstrated the measurement of real-time forces and three-dimensional kinematics, for at-scale flapping wings. Because the wings are mechanically driven, it is possible to precisely control experimental parameters in ways not possible when working with live insects. Since the experiments are at-scale, actual insect wings can be tested. The demonstrated quality of the measured forces motivates future work focused directly on the aerodynamics. Methods to more precisely control flapping kinematics, combined with flow visualization techniques, will compliment existing capabilities in measuring and understanding detailed wing deformations and real-time forces.

# Chapter 3

# Flapping-Wing MAV Conceptual Design

## 3.1 Introduction

The work in this thesis is a continuation of work by Wood [49] in developing the Harvard Microrobotic Fly (HMF). To design this device, Wood pursued a simple, yet elegant strategy. He chose the total mass for the vehicle (100 mg), and then designed an actuator optimized for high energy density with a mass somewhat less to leave room for a battery, airframe, etc. Then he looked at morphology data for actual insects, and selected a flapping frequency common for insects of this mass (Diptera, 120 Hz). With a chosen actuator stiffness and flapping frequency, he sized the wing such that its inertia was low enough to flap at resonance at this frequency. The passive wing hinge was sized by trial-and-error to achieve an optimal amount of wing rotation. While batteries are not yet available to achieve untethered flight

at this mass, Wood's original design has been very successful, not only by his clever engineering, but from the hints provided by nature.

In spite of this success, such bio-mimicry methods don't carry any guarantee of optimal performance, and without a more formal process, the influence of each design parameter (wing length, vehicle mass, flapping frequency, etc.) on each performance metric (flight endurance, speed, etc.) is not evident. It is also useful to establish design sensitivities. Should I work more on actuator efficiency or aerodynamic efficiency? Are there limits to the sizes and masses of feasible designs? This chapter develops a formal process to answer these and other questions.

When trying to model an entire system, simplifications must be made to make an analytical (or even numerical) solution tractable. The approximations of this vehicle design model have been carefully chosen to preserve the influence of all relevant design parameters which are of interest for a first-cut "clean sheet" conceptual design.

## 3.2 System dynamics

We shall model the actuator-transmission-wing system of a flapping vehicle with an equivalent one degree-of-freedom (DOF) lumped-parameter (LP) linear model, characterized by effective mass, stiffness, and damping coefficients. We seek analytical expressions associating these coefficients with a set of independent parameters describing the properties and performance of the actuator, transmission, and wings. Figure 3.1 shows a simplified flapping configuration with a single power actuator driving two wings, and the equivalent translational LP model. We assume that the wings flap symmetrically in a horizontal stroke plane, with peak-to-peak flapping amplitude

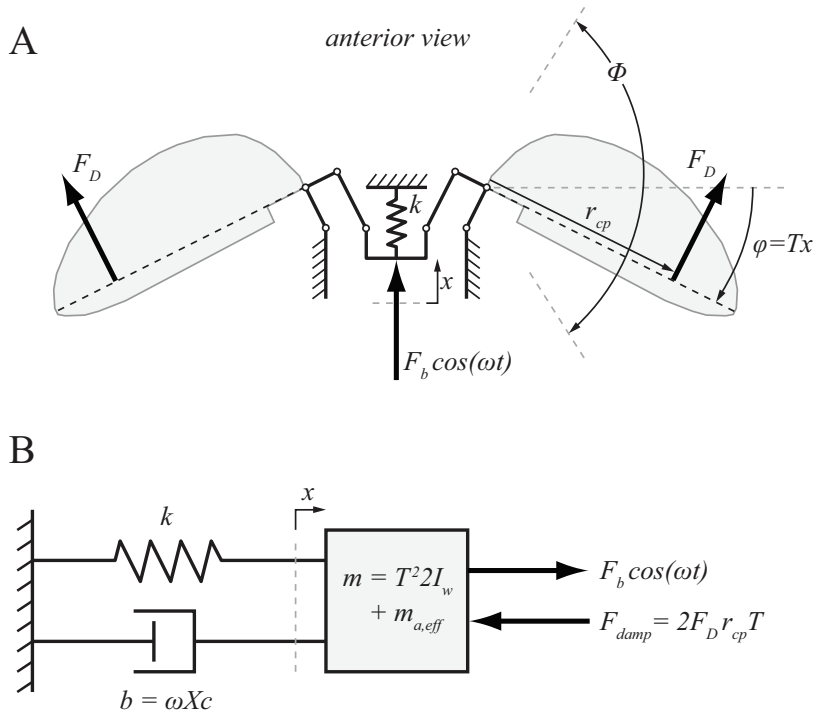


Figure 3.1: (A) Canonical flapping configuration consistent with our model: a single linear actuator drives both wings symmetrically through an (assumed) linear transmission, as viewed normal to the stroke plane. (B) Equivalent lumped-parameter (LP) linear model used in our analysis.

Φ.

The wings are coupled to the drive actuator through a linear, lossless transmission with transmission ratio $T$, where the time-varying flapping angle $\phi(t)$ and actuator displacement $x(t)$ are related by $\phi = Tx$. The drive actuator is modeled as an idealized force source, characterized by its blocked force $F_b$ and "static" or "free" deflection $\delta_{st}$. These values should be taken from operating conditions if DC measurements degrade at high frequencies. The effective mass $m$ is the sum of the actuator effective mass $m_{a,eff}$ and the effective mass of the wings $2I_wT^2$, where $I_w$ is the mass moment

of inertia of a single wing.

With the effective mass $m$ and stiffness $k = F_b/\delta_{st}$ in hand, we need only the damping coefficient $b$ to complete our LP model. Damping results from aerodynamic drag, labeled $F_D$ in figure 3.1, acting through the aerodynamic center of pressure at radial position $r_{cp}$. We use the blade-element model from chapter 2 to estimate lift and drag. The damping force seen by the actuator during symmetric flapping is twice the drag of one wing, reflected through the transmission,

$$F_{damp} = 2F_D\hat{r}_{cp}RT, \tag{3.1}$$

where $\hat{r}_{cp}$ is the non-dimensional radial position of the centre of pressure ($\hat{r}_{cp} = r_{cp}/R$). For a linear model, the damping force must be proportional to $\dot{\phi}$, but there is a $\dot{\phi}^2$ dependence on $F_D$. We replace the quadratic term $\dot{\phi}^2$ with $\dot{\phi}_0\dot{\phi}$, where $\dot{\phi}_0$ is the angular velocity at mid-stroke ($\phi = 0$). This "secant" approximation is a standard way to cope with a quadratic damping term [34].

Sinusoidal excitation, $F_b\cos(\omega t)$, results in a displacement $X\cos(\omega t - \phi_p)$, where $X$ is the amplitude of linear translation, with phase $\phi_p$. Using $\dot{\phi} = T\dot{x}$ and $\dot{\phi}_0 = \omega XT$ we find that $F_{damp} = \omega Xc\dot{x}$ and $b = \omega Xc$, where

$$c = T^3\rho\widetilde{C}_D\frac{R^5}{\mathcal{R}}\hat{r}_2^2\hat{r}_{cp}. \tag{3.2}$$

Notice that the damping coefficient $b$ is a parametric function of the solution amplitude and frequency. Since it does not depend on $x$—only the parameters $X$ and $\omega$—the LP model is still linear. Parametric dependence of $b$ ensures the correct value of $\dot{\phi}_0$ is used in the approximation for different flapping amplitudes and frequencies.

Since $c$ must be constant, $C_D(\alpha)$ has been replaced with $\widetilde{C}_D \equiv C_D(\alpha_0)$, where $\alpha_0$ is the angle-of-attack at mid-stroke. Since $C_D$ is fixed to the midstroke value, we expect

errors in $F_{damp}$ away from $\phi = 0$. In figure 3.2, the actual drag, computed using (3.1) for sinusoidal flapping and rotation, is compared against the secant approximation (dashed) for a range of values of $\alpha_0$. Notice how the faults of fixed $C_D$ are offset by our previous fault in assuming $\dot{\phi}^2 \rightarrow \dot{\phi}_0\dot{\phi}$, particularly for $\alpha_0 = 35°$ and $\alpha_0 = 45°$. Away from mid-stroke we underestimate $\alpha$ (drag prediction low) and overestimate $\dot{\phi}^2$ (drag prediction high). For high wing pitching (small $\alpha_0$), a significant under-prediction of drag levels occurs away from $\phi = 0$. With less pitching ($\alpha_0$ large) the velocity error dominates, and drag is over-predicted.

We now have analytical expressions for all the coefficients in our LP model,

$$m\ddot{x} + \underbrace{\omega X c}_{\text{“}b\text{”}}\dot{x} + kx = F_b \cos(\omega t). \tag{3.3}$$

The solution is computed using the usual methods, giving

$$\hat{X} = \frac{q^2}{r^2}\left[-\frac{(1-r^2)^2}{2} + \sqrt{\frac{(1-r^2)^4}{4} + \frac{r^4}{q^4}}\ \right]^{1/2}, \tag{3.4}$$

where $\hat{X}$ is $X/\delta_{st}$ and $r = \omega/\omega_n$, with $\omega_n = \sqrt{k/m}$ the natural frequency. The constant $q$ is defined to be

$$q = \sqrt{\frac{mk}{cF_b}} = \sqrt{\frac{m}{c\delta_{st}}}. \tag{3.5}$$

We assume hereafter that flapping in hover is designed to occur at the natural frequency $\omega_n$, unburdening the actuator from the task of storing and returning negative power. At $r = 1$, $\hat{X} = q$; thus, $q$ is, by one common definition, the quality factor for this system.

Experiments show that a linear LP model captures the primary resonance of symmetric-flapping insect-scale MAVs [19]; high frequency behavior resulting from structural modes, nonlinear harmonics and rotational dynamics are not captured.

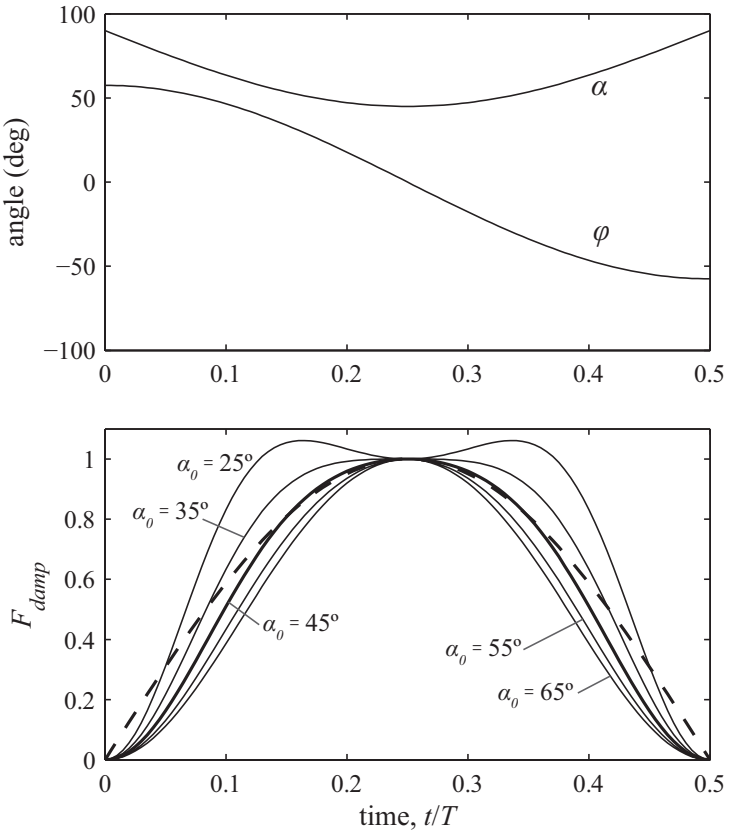


Figure 3.2: Our conceptual design model assumes sinusoidal flapping and symmetric sinusoidal wing pitching. One half of a flapping period is plotted, with $\Phi = 115°$ and $\alpha_0 = 45°$. In the lower plot, damping force (arbitrary units) due to drag (solid) is compared with the linear damping force (dashed) obtained with the secant approximation ($\dot{\phi}^2 \to \dot{\phi}_0\dot{\phi}$ and $C_D(\alpha) \to C_D(\alpha_0)$).

## 3.3 Energetics of hovering

With a model and solution for the dynamics of flapping, we can begin our conceptual design. For a vehicle of a given wing radius $R$ and weight $W$, we size the actuator by first determining the required blocked force. At the natural frequency, $\hat{X} = q$; when combined with (3.5) we find

$$F_b = c\omega_n^2 X^2. \tag{3.6}$$

Note that we can easily transform any expression into its rotational equivalent; here, $F_b = c\omega_n^2 \Phi^2/(2T)^2$. We define the total and static total flapping angles (peak-to-peak), $\Phi \equiv 2TX$ and $\Phi_{st} \equiv 2T\delta_{st}$. To determine the required flapping frequency we employ the constraint that at hover, $W = 2L$, where $W$ is the total vehicle weight and $L$ is the stroke-averaged lift (thrust) generated by each wing, defined by our conventions as the net vertical aerodynamic force. Substitute (2.20) into (2.22) and take the average over one half-period,

$$L = \frac{1}{2}\rho \frac{R^5}{\mathcal{R}} \hat{r}_2^2 \frac{1}{\pi} \int_0^\pi C_{L_{max}} \sin(2\alpha(s)) \dot{\phi}_0^2 \cos^2(s) ds. \tag{3.7}$$

This yields

$$L = \frac{1}{2}\rho \frac{R^5}{\mathcal{R}} \hat{r}_2^2 \frac{1}{2} \widetilde{C}_L \omega^2 T^2 X^2, \tag{3.8}$$

where we have defined a mean lift coefficient

$$\widetilde{C}_L \equiv C_{L_{max}} \frac{2}{\pi} \int_0^\pi \sin(2\alpha(s)) \cos^2(s) ds. \tag{3.9}$$

We do not incorporate the factor of $1/2$ seen leading $\widetilde{C}_L$ throughout the paper because it represents the $\cos^2(\omega t)$ reduction in lift that results from sinusoidal flapping. If we assume that wing pitching is also sinusoidal, then $\widetilde{C}_L = 0.94 C_{L_{max}}$ for the case

$\alpha_0 = 45°$; the reduction in effective $C_L$ is largely due to the sinusoidal flapping profile and not wing pitching.

We substitute $L = W/2$ into (3.8) and rearrange to find the angular flapping frequency required to maintain steady hover

$$\omega_n = \frac{1}{\hat{r}_2 R^2 \frac{1}{2}\Phi}\sqrt{\frac{\cancel{R}W}{\frac{1}{2}\widetilde{C}_L \rho}}. \tag{3.10}$$

After substituting (3.2) and (3.10) into (3.6) we obtain the required blocked force

$$F_b = TW\frac{\widetilde{C}_D}{\frac{1}{2}\widetilde{C}_L}\hat{r}_{cp}R. \tag{3.11}$$

This simple result makes sense intuitively; the blocked force the actuator must supply is proportional to the mean drag force, which is simply the vehicle weight divided by $L/D$. The quantity $T\hat{r}_{cp}R$ represents magnification of the drag force through the transmission. In the wing-frame, the blocked torque is $Q_b = F_b/T$.

### 3.3.1 Sizing the actuator

To develop a mass budget, we divide total vehicle mass $m_t$ into $m_t = m_p + m_b + m_a$, the sum of payload, battery, and actuator masses. Here, "payload" refers to all non-useful mass, including structure, sensors, control actuators, electronics, etc. Any vehicle components which are not the actuator and battery must be accounted for. We also define mass fractions $\mu_p = m_p/m_t$, etc., for these components.

Lacking extensive data from successful designs, we shall assume a fixed value for $\mu_p$ and decide how to divide the remaining mass budget $1 - \mu_p$ between the actuator and battery. The actuator is sized to deliver the required $\delta_{st}$ and $F_b$. Any remaining

mass is left to the battery, $\mu_b = 1 - \mu_p - \mu_a$. Under this scheme, we have made $\mu_a$ an independent variable; vehicle performance will drive its selection.

To develop a model for actuator mass, we follow the approach of [25], in which the actuator is sized based on the energy it must deliver each flapping period and the energy density $S_a$ (i.e. J/kg) characteristic to actuators of its type. For a linear bimorph actuator, this balance is given by

$$m_a S_a = F_b \delta_{st}. \tag{3.12}$$

If the actuator requires power electronics or amplifier circuitry, then the mass of these components must be accounted for by including them in $\mu_p$ or by reducing $S_a$.

It is very important to clarify that with this expression we are assuming a type of actuator in which the actuation frequency and the flapping frequency are required to be the same. This includes piezoelectric, electrostatic, SMA, EAP, and other linear[1] strain-based actuators. Pneumatic, chemical, and insect flight muscles are other examples. The only actuators that do not qualify are rotary-type (motors) which can use a gearbox to decouple the actuation frequency from the flapping frequency. The major weakness of linear actuators is that their power density will drop as flapping frequency drops, while a motor can maintain peak power output and power density with a gearbox.

If a motor is used, the designer might consider a helicopter MAV over a flapping-wing MAV, especially for larger vehicles. There is some indication that revolving wings outperform flapping wings in hover [28], but in practice, the superiority of

[1]Here "linear" refers to "action along a straight line", not linearity of an actuator's input-output relationship.

either approach has not been demonstrated conclusively for gram-scale and sub-gram MAVs. Since helicopter design is not the focus of this paper, we will primarily consider linear actuators, which are not appropriate for helicopter configurations.

Returning to (3.12), we substitute (3.11) to obtain

$$\mu_a = \frac{g}{S_a}\frac{\widetilde{C}_D}{\widetilde{C}_L}\hat{r}_{cp}R\Phi_{st}. \tag{3.13}$$

Based on this relationship, $\mu_a$ is no longer an independent design parameter—its value is set when the designer selects $R$. Note that $\mu_a$ does not depend on vehicle weight, but increases linearly with $R$. This means that for $R$ large enough, no feasible design is possible; as $R$ increases, $\mu_a$ grows until $\mu_a = 1-\mu_p$, consuming all available vehicle mass and leaving no room for a battery. This critical wing radius $R_{crit}$ sets an upper bound on the size of the flapping vehicle, independent of vehicle mass,

$$R_{crit} = \frac{(1-\mu_p)}{\Phi_{st}\hat{r}_{cp}}\frac{\widetilde{C}_L}{\widetilde{C}_D}\frac{S_a}{g}, \tag{3.14}$$

and thus the actuator mass fraction becomes

$$\mu_a = (1-\mu_p)\frac{R}{R_{crit}}. \tag{3.15}$$

There is a limit to how small $\mu_p$ can be reduced and $L/D$ maximized; $R_{crit}$ depends primarily on the energy density of the actuator technology. To get an idea of the magnitude of $R_{crit}$ we can make a few rough assumptions, namely: $\mu_p = 0.25$; $\hat{r}_{cp} = 0.6$, this value is representative of typical insect wings [15]; sinusoidal flapping with $\Phi = \Phi_{st} = 115°$ and symmetric sinusoidal wing pitching with $\alpha_0 = 45°$, which yields $\widetilde{C}_L = 1.8$ and $\widetilde{C}_D = 1.9$ from the robofly coefficients and equations (2.20) and (3.9); $S_a = 1.5$J/kg: this value is chosen because it is representative of both insect flight

muscle [14] and piezoelectric bimorph actuators [51]. With these numbers (on Earth, $g = 9.8\text{m/s}^2$) we obtain $R_{crit} = 91\text{mm}$. With less payload, better aerodynamic efficiency or higher actuator energy density, larger-winged vehicles are possible.

For this example we have chosen $q = 1$ ($\Phi = \Phi_{st}$). It appears that a design with $q > 1$ ($\Phi$ held constant) will reduce actuator mass and allow designs with larger wings. Whether this is true or not depends on the details of the actuator. For example, piezoelectric actuators are typically strain limited, not field limited, so raising $q$ results in an equivalent reduction of $S_a$. You can reduce $\Phi$ and $\Phi_{st}$ both, maintaining $q = 1$, but experiments have shown that reducing flapping amplitude is aerodynamically inefficient. The issue of high-$q$ designs is complex, and demands independent attention.

### 3.3.2 Flight endurance

We know the required actuator mass fraction, but which $R$ and $W$ do we pick? Answering this requires a performance goal. We start by identifying designs that maximize flight endurance, and later address flight speed and range. Endurance is a good starting point because it speaks directly to the feasibility of a hovering MAV. The expression for hover endurance is simply

$$t_f = \frac{S_b m_b}{P/\eta}, \tag{3.16}$$

where $S_b$ is the battery energy density, $\eta$ is the electrical-to-mechanical efficiency of the actuator and associated power electronics, and $P$ is the mechanical power consumed in flapping the wings. From our dynamic model of flapping, the expression

for power consumption at $r = 1$ is

$$P_n = \frac{1}{2} F_b \omega_n X. \tag{3.17}$$

Substituting $F_b$ and $\omega_n$ using (3.11) and (3.10) gives

$$\frac{P_n}{W} = \sqrt{2} \frac{\widetilde{C}_D}{\widetilde{C}_L^{3/2}} \frac{\hat{r}_{cp}}{\hat{r}_2} \sqrt{\frac{\mathcal{A}RW}{\rho R^2}}. \tag{3.18}$$

This expression is ubiquitous in aircraft design—nearly identical forms exist for airplanes and rotorcraft: $P/W$ is proportional to the square root of *wing loading* or *disk loading*, defined as $W/S$, where $S$ is an airplane's total wing area or the area swept by a helicopter's main rotor. Since $t_f$ is proportional to $W/P_n$, it is clear that minimizing wing loading is critical to maximizing flight endurance. After substitution, we obtain the following expression for flight endurance,

$$t_f = \frac{\sqrt{2}}{2} \eta \frac{S_b}{g} \frac{(1-\mu_p)}{\sqrt{W}} \frac{\widetilde{C}_L^{3/2}}{\widetilde{C}_D} \frac{\hat{r}_2}{\hat{r}_{cp}} \sqrt{\frac{\rho}{\mathcal{A}}}\, R\left(1 - \frac{R}{R_{crit}}\right). \tag{3.19}$$

The dependence of flight endurance on wing radius is illustrated by figure 3.3. For a wing radius $R^* = R_{crit}/2$, flight endurance is maximized. This quadratic dependence on $R$ results from two conflicting requirements: minimizing $R$ minimizes $\mu_a$, increasing available battery energy; maximizing $R$ minimizes wing loading, reducing the power required to hover. When $R = R^*$, actuator and battery mass fractions are identical,

$$\mu_a^* = \mu_b^* = \frac{1 - \mu_p}{2}, \tag{3.20}$$

and the expression for maximum flight endurance is

$$t_f^* = \frac{\sqrt{2}}{8} \eta \frac{S_a}{g} \frac{S_b}{g} \frac{(1-\mu_p)^2}{\sqrt{W}} \frac{\widetilde{C}_L^{5/2}}{\widetilde{C}_D^2} \frac{\hat{r}_2}{\hat{r}_{cp}^2} \sqrt{\frac{\rho}{\mathcal{A}}} \frac{1}{\Phi_{st}}. \tag{3.21}$$

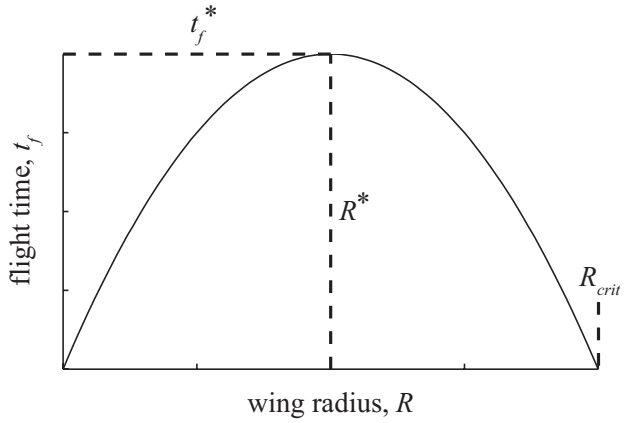


Figure 3.3: For a given vehicle weight, flight endurance depends quadratically on wing length. When $R = R_{crit}$, $\mu_a = 1 - \mu_p$, leaving no room for a battery, resulting in a flight time of zero. Maximum flight time $t_f^*$ occurs at $R^* = R_{crit}/2$.

Why is there an inescapable reduction in $t_f$ as $W$ increases? Flight time is inversely proportional to $P/W$. Notice from (3.18) that maintaining $P/W$ while increasing $W$ requires holding the wing loading constant; if we increase $W$, a concomitant increase in $R^2$ is required. Increasing $R$, however, is not possible; when raised above $R_{crit}$, savings from reduced power consumption are more than wiped out by the decrease in flight time resulting from a smaller battery.

With a few more assumptions, we can generate representative flight endurance numbers: we assume $\eta = 10\%$, a figure again in line with piezoelectric actuators and insect flight muscles [51][14]; $\hat{r}_2 = 0.56$ and $\text{Æ}R = 4$, characteristic values for insect wings [15]; $S_b = 500\text{kJ/kg}$, a typical value for lithium polymer batteries [25]; air density $\rho = 1.2\text{kg/m}^3$. Our choice for $S_b$ may be optimistic because we do not account for capacity derating during high C-rate discharges.

In figure 3.4 we plot flight endurance over $R$ and $m_t$. Flight endurance continues

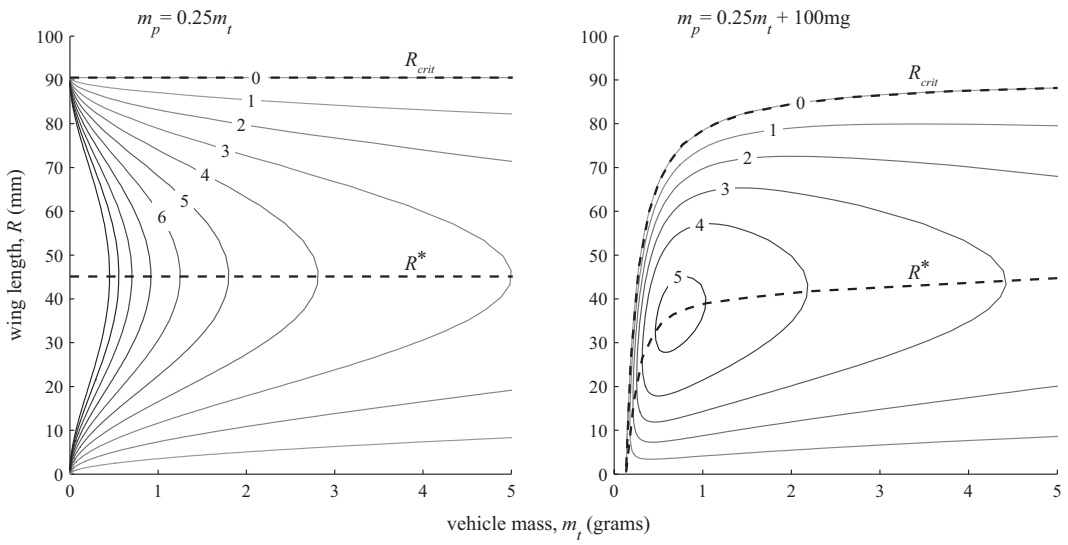


Figure 3.4: Flight endurance (plotted in minutes) for two different payload mass models. A fixed payload requirement results in a local maximum in flight endurance. Assumed performance values for the battery, actuator, and aerodynamics are given in the text.

to increase as $m_t$ decreases. Our assumption of constant lift and drag coefficients breaks down for $Re$ less than about 100, which corresponds to a vehicle mass of about 1mg. Variation of other parameters we have assumed to be constant is likely, such as a probable increase of $\mu_p$ as $W$ drops. Fabrication limitations prevent continuous miniaturization of vehicle components. For example, if an additional fixed payload of 100mg is applied, a local maximum for flight endurance occurs, as shown in figure 3.4. If variations in $C_L$, $C_D$, $\eta$, $S_a$, $S_b$, or $\mu_p$ with changes in $R$ and $W$ are known, either from previous designs or more sophisticated models, these results should be modified appropriately.

From these results it is clear that $\eta$ are $S_b$ are *critical* parameters, with a great potential to increase flight endurance. Insects are fortunate to carry carbohydrate or

fat energy stores with approximately 50 times the energy density of lithium polymer batteries. Increasing the actuator energy density $S_a$ will increase flight time, but large improvements in $S_a$ present diminishing returns unless the designer is willing to increase $R$ to follow resulting increases in $R^*$. We'll see shortly that increasing $R$ negatively impacts flight velocity and range.

It is tempting to use these results to optimize wing shapes through variation of $\hat{r}_{cp}$, $\hat{r}_2$, and $\mathcal{AR}$. Low aspect ratios, for a fixed $R$, decrease wing loading by increasing wing area. However, low $\mathcal{AR}$ wings may suffer reduced lift and drag coefficients from increased tip loses and a reduction in chord-normalized flapping amplitude. Additionally, our simplified estimates of lift and drag do not account for induced flow effects and their dependence on wing size and shape. Detailed optimization of wing shape and flapping kinematics are second-order effects to be investigated experimentally at a later design stage.

### 3.3.3 Flight speed and range

A simple way to predict flight speeds uses the *advance ratio*, a non-dimensional parameter, $J$, defined as the ratio between forward flight speed $V$ and the mean wingtip velocity,

$$J = \frac{V}{2\Phi f R}. \tag{3.22}$$

From this expression we can estimate $V$ by assuming a "reasonable" cruise value for $J$. A recent flapping MAV capable of controlled hover and forward flight has a reported advance ratio of 0.5 at top speed [26]. As $J$ approaches and exceeds 1, our in-hover model cannot accurately predict lift and drag; a tilted stroke plane is required to

overcome rising parasitic body drag, and the relative velocity from forward flight is non-negligible in modeling wing aerodynamics. These issues will affect our ability to accurately predict power consumption and maximum range. Classically, aircraft and helicopters benefit from a reduction in induced drag as flight speed increases, but this is not universally observed in metabolic data from insects [14]. The following analysis seeks only the basic scaling of vehicle range at small $J$, assuming power consumption is constant with flight speed. We begin by substituting the flapping frequency (3.10) into (3.22) to obtain

$$V = \frac{2J}{\pi \hat{r}_2 R}\sqrt{\frac{\not{R}W}{\frac{1}{2}\widetilde{C}_L \rho}}. \tag{3.23}$$

Achieving high flight speed implies heavy vehicles with small wings. This trend toward smaller wings conflicts with the prescription for maximum flight endurance, which is to grow the wings until reaching the energy density limits of the actuator. Using the results for $V$ (3.23) and $t_f$ (3.19), an estimate of range $d_{max}$ is obtained,

$$d_{max} = \eta \frac{2J}{\pi}\frac{S_b}{g}\frac{\widetilde{C}_L}{\widetilde{C}_D}\frac{1}{\hat{r}_{cp}}\left(1 - \frac{R}{R_{crit}}\right)(1 - \mu_p). \tag{3.24}$$

Range is not a function of vehicle weight $W$; it decreases linearly from a maximum at $R = 0$ (obviously pathological) to zero when $R = R_{crit}$. An endurance-optimized design achieves half the maximum theoretical range. Since flight endurance depends quadratically on $R$ in the neighbourhood of $R_{crit}/2$, a balanced design (e.g. $R = R_{crit}/4$) might trade a small endurance penalty ($-25\%$) for a larger gain in range ($+50\%$).

## 3.4 Flapping dynamics and wing structural-inertial efficiency

For every $R$–$W$ combination there is a unique flapping frequency, given by (3.10), which ensures $L = W/2$. Actuator stiffness $k = F_b/\delta_{st}$ is also fixed by this combination; wing inertia is then set to achieve the required frequency $\omega_n = \sqrt{k/m}$. Since wing inertia cannot be reduced indefinitely, there may be regions of the design space where hover cannot be achieved. To explore this limitation, we need a predictive model for wing mass moment of inertia $I_w$ as a function of $R$ and $W$.

Lightening the wings will negatively impact their structural performance. To determine the lightest feasible wings we must establish a wing stiffness criteria. We model each wing as a beam with mean cross-sectional area $A_c$, length $R$, and mean density $\rho_w$. Under these assumptions, wing inertia $I_w$ scales as

$$I_w \propto \rho_w A_c R^3. \tag{3.25}$$

Bending stiffness requirements determine $A_c$. The actual loading and deflection of a wing is very complex; we are only interested in how wing deflection scales with changes in wing length $R$ and vehicle weight $W$. To assess wing stiffness, we hypothetically clamp the wing at its base and load it at the tip with a force equal to the vehicle weight $W$, and measure the resulting tip deflection $w$. The Euler-model of beam-bending yields

$$w \propto \frac{WR^3}{E_w I_{w,a}}, \tag{3.26}$$

where $E_w$ is the Young's modulus and $I_{w,a}$ is the second moment of area of the beam

cross-section. Following Ashby [4], we write the second moment of area as

$$I_{w,a} = I_0 \phi_B^e = \frac{A_c^2}{4\pi} \phi_B^e, \tag{3.27}$$

where $I_0$ is the second moment of area of a circle, and $\phi_B^e$ is the *shape factor* of the beam cross-section. High-efficiency shapes, such as I-beams, have a large shape factor; corrugations in insect wings contribute to a high shape factor. We substitute this expression into (3.26), substitute the non-dimensional tip deflection $\hat{w} = w/R$, and solve for cross-sectional area:

$$A_c \propto \frac{\sqrt{W} R}{\sqrt{E_w \phi_B^e \hat{w}}}. \tag{3.28}$$

Substituting into (3.25) we obtain,

$$I_w = \frac{\sqrt{W} R^4}{\mathcal{M}_1}, \tag{3.29}$$

where we have defined,

$$\mathcal{M}_1 \equiv \phi_w \frac{\sqrt{E_w}}{\rho_w} \sqrt{\hat{w}}, \tag{3.30}$$

a performance measure of the wing's structural efficiency, which we seek to maximize. The term $\phi_w$ is an over-all measure of wing structural-inertial efficiency, encompassing $\phi_B^e$ and efficiency improvements from wing tapering. We recognize $\sqrt{E_w}/\rho_w$ as the classic material selection figure-of-merit for bending stiffness [4]. Permitting more tip deflection (larger $\hat{w}$) reduces the stiffness requirement and allows wings with lower inertia (larger $\mathcal{M}_1$). We cannot easily calculate $\mathcal{M}_1$. This would require detailed knowledge of the shape and mass distribution of the wing, and determination of acceptable tip deflection $\hat{w}$. For a conceptual design, it is much easier to empirically determine $\mathcal{M}_1$ from insect and artificial wing data using (3.29). If our scaling assumptions are correct, $\mathcal{M}_1$ will show little variation with $R$ and $W$, as it represents

a wing "technology factor" with respect to inertial and structural efficiency. With a representative value for $\mathcal{M}_1$, we can estimate the minimum achievable wing inertia for each $R$–$W$ combination.

Insect wing data is a good source for testing the scaling prescribed by (3.29); using data from reference [15], figure 3.5 plots $\mathcal{M}_1$, derived from reported values of $R$, $W$, and $I_w$. Also included is a carbon fibre artificial wing, as reported in [30]; for this wing, $W$ is set to the maximum lift obtained from a pair of these wings in tethered flight testing. This wing is representative of the "state-of-the-art" in artificial wing fabrication; the spars are laser-cut unidirectional ultra-high modulus (UHM) carbon fiber prepreg, cured and bonded to a 1.5$\mu$m polyester film. While bending tests have confirmed that these wings are comparable in stiffness to similarly-sized natural wings [45], their moment of inertia is higher, yielding low $\mathcal{M}_1$ values ($\sim 70$) relative to most natural insect wings.

This $I_w$-scaling analysis is one of many plausible schemes. For example, it could be assumed that wing cross-sectional area scales with $R^2$ or that wing inertial loads drive bending stiffness criteria; basic dimensional analysis might predict $I_w \sim WR^2$. We could not, however, find an alternative scaling method with better correspondence to published insect wing data. Figures-of-merit derived from these schemes showed much stronger dependence on $R$ and $W$. Future work in optimizing wing structural-inertial efficiency may improve our understanding of the scaling of $I_w$—particularly with respect to artificial wings—but the chosen scaling is adequate for the conceptual design phase.

With an estimate for the minimum achievable $I_w$, the maximum achievable flap-

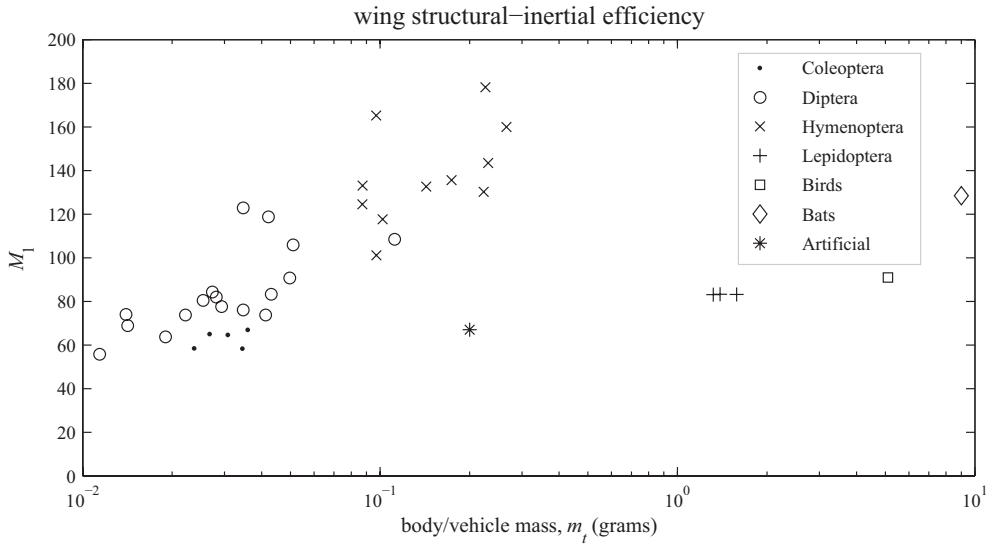


Figure 3.5: Wing figure-of-merit $\mathcal{M}_1$, as calculated from data in ref. [15], for all nominally two-wing insects with $I_w$ measurements available. The bird (*Amazilia fimbriata fluviatilis*) and bat (*Plecotus auritus*) are both capable of hover. Artificial wing data as reported in [30]. Units of $\mathcal{M}_1$ are $\mathrm{m}^{5/2}\mathrm{kg}^{-1/2}\mathrm{s}^{-1}$.

ping frequency is $\omega_{max} = \sqrt{\kappa/(2I_w + m_{a,eff}T^{-2})}$, where $\kappa = k/T^2$. Comparing this maximum frequency with the required frequency (3.10), we obtain a *minimum* wing radius,

$$R_{min} = \frac{\Phi_{st}\mathcal{AR}\sqrt{W}}{\mathcal{M}_1\hat{r}_{cp}\hat{r}_2^2\widetilde{C}_D\rho\frac{1}{4}\Phi^2}, \tag{3.31}$$

where we have assumed that the actuator effective mass is a negligible contributor to overall effective mass. This assumption is tested for high mass vehicles, but achievable transmission ratios—up to 3 rad/mm in a single-stage flexure-based transmission is feasible without extraordinary effort—are sufficient to reduce actuator effective mass to an insignificant level.

For a given $W$, designs with a wing radius below $R_{min}$ cannot flap with a natural frequency high enough to generate sufficient lift to hover. Figure 3.6 repeats the performance plots of figure 3.4 with equation (3.31) overlaid. Feasible designs must lie *above* the inertia-limit curves. For large enough $\mathcal{M}_1$, maximum endurance is not restricted, but fast or heavy long-range designs may still be limited. Where the inertia-limit curve crosses the horizontal line $R = R_{crit}$, we find a hard upper-bound on vehicle weight,

$$W_{max} = \left[\mathcal{M}_1(1-\mu_p)\frac{S_a}{g}\frac{\widetilde{C}_L\hat{r}_2^2\rho}{4\mathcal{AR}}\left(\frac{\Phi}{\Phi_{st}}\right)^2\right]^2. \tag{3.32}$$

Using our previously-set representative values, we find maximum vehicles masses of 12 and 20 grams for $\mathcal{M}_1 = 70$ and $\mathcal{M}_1 = 90$, respectively. While it is exciting to speculate on the implications of this equation, particularly with respect to establishing an upper bound on, say, hummingbird mass, the quadratic dependence on nearly all parameters, especially $S_a$, $M_1$, and $\mu_p$, precludes accurate predictions. On the other hand, the scaling trend is clear: there *are* limits on the maximum feasible weight for

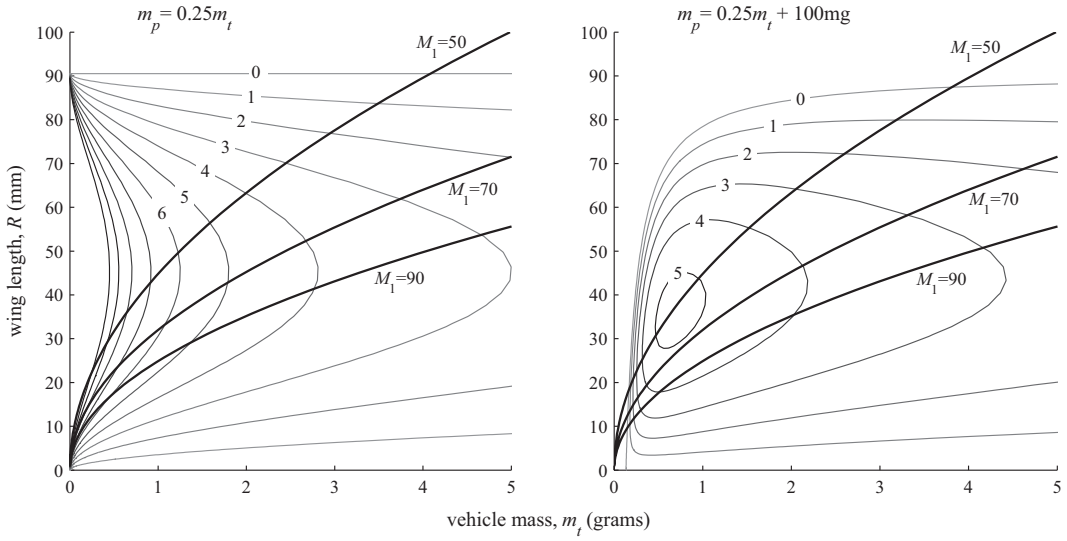


Figure 3.6: Wing structural-inertial limits, for different values of the $\mathcal{M}_1$ figure-of-merit overlay flight endurance results from figure 3.4. Feasible designs must lie *above* these curves.

hovering MAVs.

The existence of large helicopters appears to contradict this result. We determined $W_{max}$ by equating the expressions for $R_{min}$ (3.31) and $R_{crit}$ (3.14). However, $R_{crit}$ is only defined for linear-type actuators; if a motor-and-gearbox drive the wings, this expression does not apply. If the actuator is characterized by its power density, $S'_a$, then the actuator-sizing equation—(3.12) for linear-type actuators—is replaced with $P_n = S'_a \mu_a m_t$, and the expression for actuator mass fraction becomes

$$\mu_a = \frac{g}{S'_a} \frac{P_n}{W}, \tag{3.33}$$

There is no upper-limit on $R$; as wing length increases, actuator size and aerodynamic power decrease monotonically. From (3.33) it is straightforward to re-derive expressions for flight endurance and range. However, previous results for aerodynamic

power (3.18) and flight speed (3.23) remain the same. Wing inertial-structural limits, and the expression for $R_{min}$ are also unchanged.

## 3.5 Wing optimization

From these results it is clear that simply maximizing $\widetilde{C}_L$ is not sufficient to achieve maximum performance. Equations 3.19 and 3.21 indicate that a wing which maximizes $\widetilde{C}_L^{3/2}/\widetilde{C}_D$ or $\widetilde{C}_L^{5/2}/\widetilde{C}_D^2$, respectively, will achieve maximum performance. These expressions also prescribe a particular combination of $\hat{r}_{cp}$, $\hat{r}_2$ and $\mathcal{AR}$ for maximizing flight endurance. However, the highly three-dimensional nature of the flow-field calls into question the validity of the cutting the wing into strips, assuming completely two-dimensional sectional flow, and integrating radially. The force scaling is most likely correct, but the leading order constants are not necessarily of great predictive value.

When testing different wings, we will report nondimensional coefficients using equation 2.18, rather than the more complex form of equation 2.22. With a reference velocity $V$ equal to the mean tip velocity $2\Phi f R$, and a reference area $S = R\bar{c}$, we obtain

$$\bar{C_L} = \frac{\mathcal{AR}\bar{L}}{2\rho\Phi^2 f^2 R^4} \tag{3.34}$$

and, for the mean power consumption, we define

$$\bar{C_P} = \frac{\mathcal{AR}\bar{P}}{4\rho\Phi^3 f^3 R^5}. \tag{3.35}$$

$\bar{L}$ is the mean lift and $\bar{P}$ is the mean aerodynamic power consumption. We have defined $\bar{C_P}$ through the expression $\bar{P} = \bar{C_P} p_{dyn} S V$. With these definitions, it is

straightforward to derive alternative forms to 3.19 and 3.21 more amenable to the reduction of experimental data,

$$t_f = \eta S_b \sqrt{\frac{\rho}{2\text{Æ}W}} \frac{(1-\mu_p)}{g} \frac{\bar{C_L}^{3/2}}{\bar{C_P}} R \left[1 - \frac{R}{R_{crit}}\right], \tag{3.36}$$

$$t_f^* = \eta \frac{S_a S_b}{g^2} \sqrt{\frac{\rho}{2\text{Æ}W}} \frac{(1-\mu_p)^2}{4\Phi} \frac{\bar{C_L}^{5/2}}{\bar{C_P}^2}. \tag{3.37}$$

Thus, the relevant figures of merit are $\bar{C_L}^{3/2}/(\bar{C_P}\sqrt{\text{Æ}})$ and $\bar{C_L}^{5/2}/(\bar{C_P}^2\Phi\sqrt{\text{Æ}})$. Lowering Æ is advantageous because, for a fixed wing length, this indicates a larger wing area, and therefor a lower wing loading. In these experiments we only considered $\bar{C_L}^{3/2}/(\bar{C_P}\sqrt{\text{Æ}})$ as a figure of merit because of technical limitations that prevented us from testing all wings over a large enough range of $\Phi$ to allow a fair comparison based on the latter figure-of-merit.

These results indicate that a low aspect ratio (large area) wing flapped at as low a total flapping angle $\Phi$ as possible is optimal. However, both of these conditions, in the extreme, will likely lead to unfavorable aerodynamics and thus a drop in $\bar{C_L}$ and a rise in $\bar{C_P}$.

### 3.5.1 Experimental setup

The experimental setup from chapter 2 was modified in a few ways. First, an optical displacement sensor was installed, allowing real-time monitoring of the flapping angle via a measurement of the actuator deflection. A calibration table was constructed mapping the actuator deflection to the flapping angle, $\phi$. Additionally, isolating amplifiers and precision shunt resistors were installed, allowing real-time measurement of the current (and therefore electrical power) flowing to the drive ac-

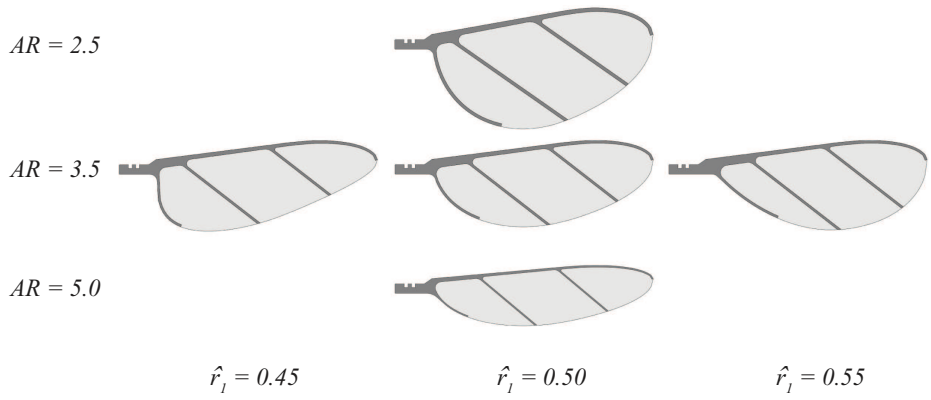


Figure 3.7: Wings tested to investigate the influence of aspect ratio and shape.

tuator. To remove the effect of dielectric losses, a large calibration set was taken by driving the actuator over a wide frequency range at several voltages, with no wing attached. These power measurements were subtracted from power values taken when driving a wing.

Figure 3.7 shows the five different wings tested. They all have $R = 15$mm, and their aspect ratios and $\hat{r}_1$ values were selected to cover a common range spanned by actual insect wings [15]. For each $\hat{r}_1$, the value of $\hat{r}_2$ was selected using equation 2.2. Planform shape was determined by equation 2.3 for all wings. The leading edge profile was chosen arbitrarily. The wing hinge axis is positioned to intersect the wing tip. Spar thickness was chosen based on experience with wings of similar size, thickened slightly to ensure the wings remained flat during testing, so as to remove that variable from consideration.

All wings used the same wing hinge, and were flapped over a wide range of fre-

quencies at several operating voltages. Each test consisted of a sweep from 50–200 Hz or 50–300 Hz, with 10 periods for each 1 Hz step concatenated together. Averaged over each 10 period sequence, $\Phi$, $\bar{L}$ and $\bar{P}$ were measured. Figure 3.8 presents sample data for the case $\mathcal{AR} = 2.5$. As flapping frequency is increased, the wing rotates more and more. At some point, the amount of rotation leading to a maximum value of $\bar{C_L}$ is reached. Usually at a slightly higher frequency, the power factor $\bar{C_L}^{3/2}/(\bar{C_P}\sqrt{\mathcal{AR}})$ reaches a maximum. This is because optimal power efficiency results at a slightly lower angle-of-attack (higher $\psi$) than the point of maximum $\bar{C_L}$. The plot of flapping amplitude in figure 3.8-A indicates resonance. While, for testing purposes, it is highly desirable to test well below the frequency of actuator-wing resonance, the reality is that an actuator stiff enough to arrange this will lead to a large reduction in the sensor bandwidth due to increased load mass. Not only will this prevent the accurate measurement of real-time forces, but damping losses from the sensor beam itself will begin to corrupt the electrical power measurements.

Figure 3.9 presents the results from testing all five wings. Each point represents the optimal operating point from the sweep over flapping frequency. The high aspect ratio wing ($\mathcal{AR} = 5$) performs rather poorly. This might be explained by the hypothesis that since the wing chord is smaller, the wing travels more chord-lengths each flapping cycle, and is effectively translating rather than rotating, relative to the lower $\mathcal{AR}$ wings. This leads to a reduction in the vortex-stabilizing effect of centrifugal acceleration [28]. To some degree, we expect that higher $\mathcal{AR}$ wings will perform better as a result of a decrease in tip-losses, but such a phenomenon is not observed here. The lower aspect ratio wings ($\mathcal{AR} = 2.5$ and $\mathcal{AR} = 3.5$) have quite similar performance, and indicate

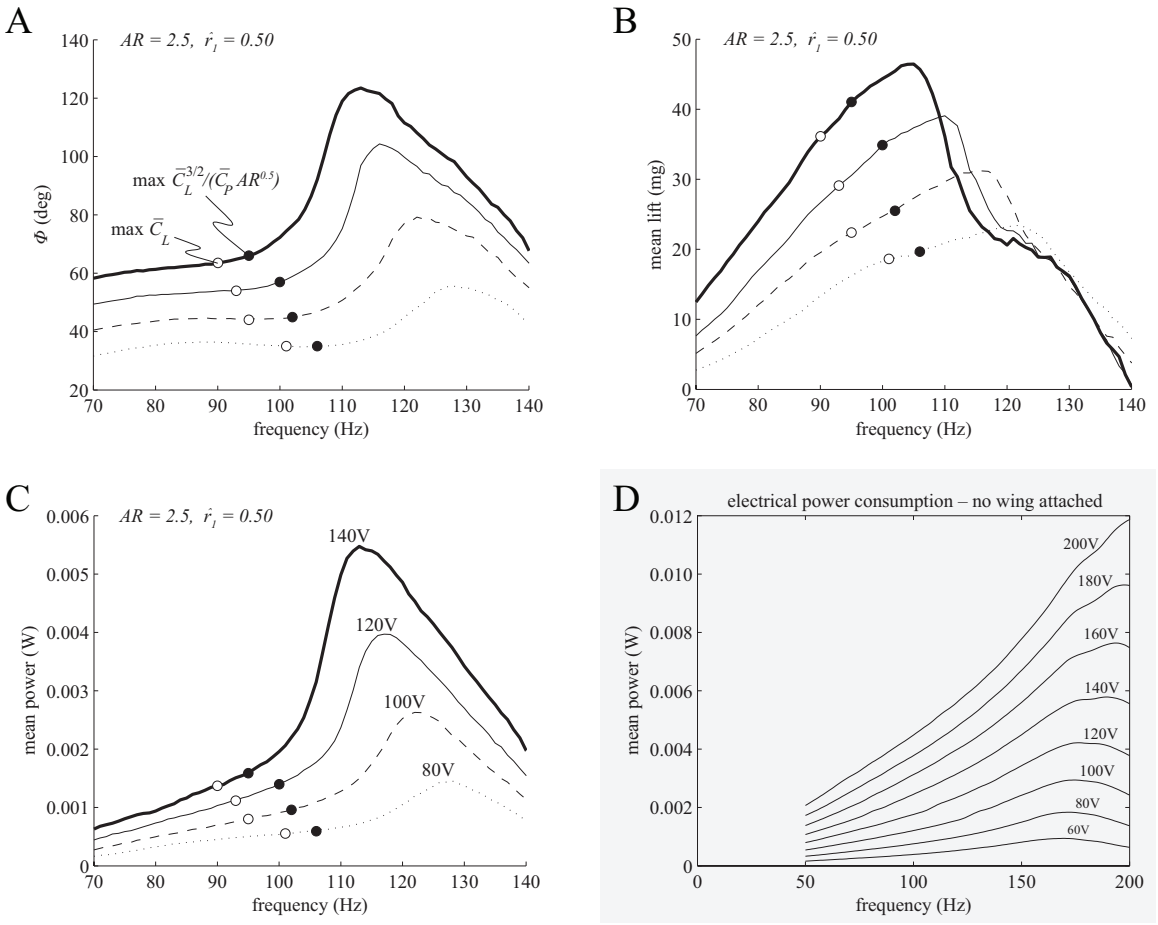


Figure 3.8: Raw test data for the $\mathcal{AR} = 2.5$ wing (A-C), and power calibration data (D).

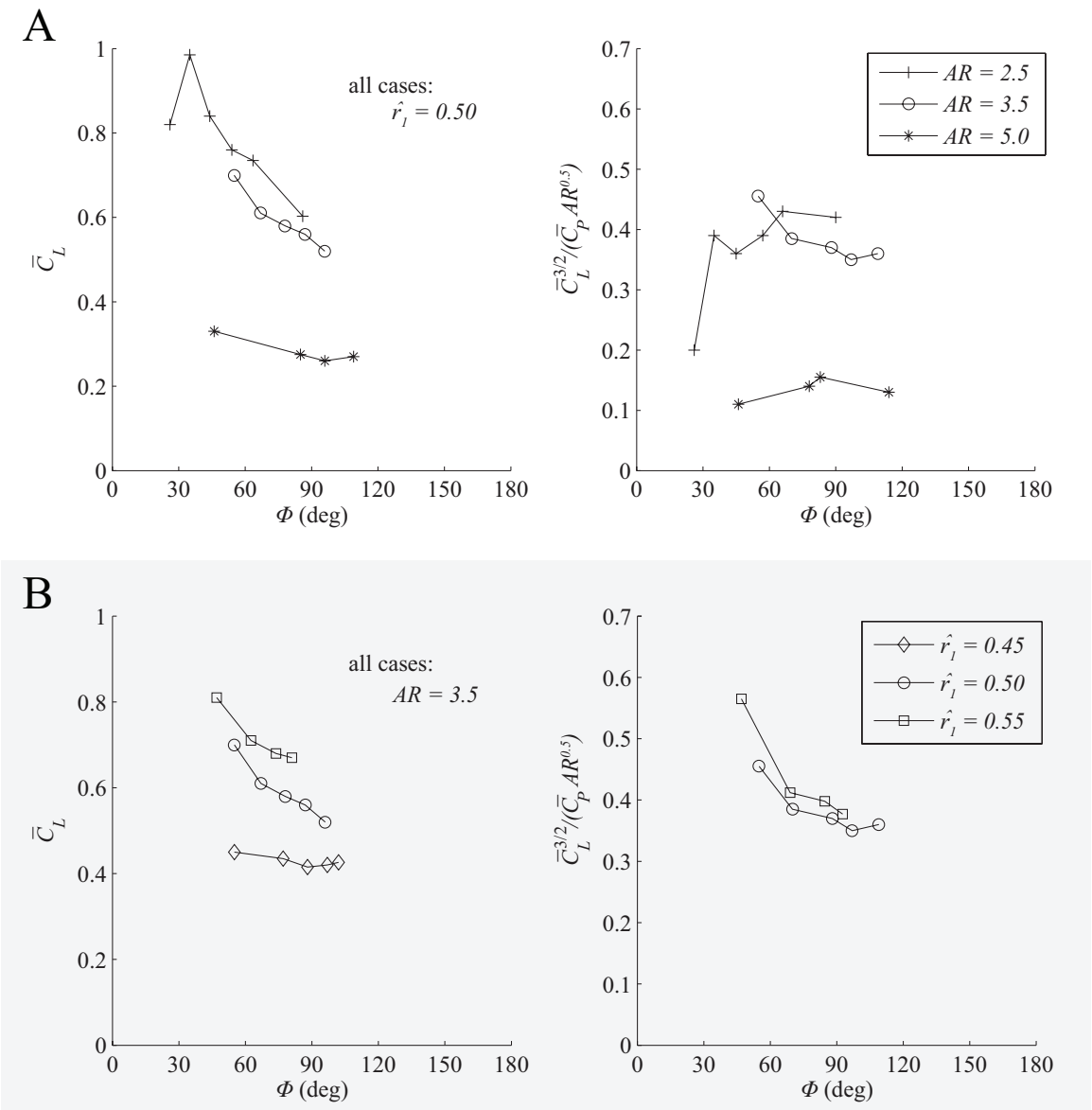


Figure 3.9: $\bar{C_L}$ and power factor for all tested wings, as a function of Φ.

additional testing with even lower aspect ratios.

There appears to be a general trend where $\bar{C}_L$ increases as flapping amplitude $\Phi$ decreases. Without detailed measurements of rotation kinematics it is difficult to speculate on the reason for this trend. Previous scaled-model experiments [28, 11] used fixed-$\alpha$ flapping kinematics during most of the mid-stroke, rather than the mostly-sinusoidal variation resulting from sinusoidally-driven passively-rotating wings. Power factor remains more or less constant over the ranges of $\Phi$ tested, and is seen to drop off precipitously for $\mathcal{AR} = 2.5$ below approximately $\Phi = 35°$. It is expected that this drop will occur at higher $\Phi$ as $\mathcal{AR}$ is decreased. We might expect an improvement in power factor as $\Phi$ increases, through a reduction in "disk loading", but again, a full understanding of the absence of this effect requires detailed measurements of $\psi(t)$. For these experiments, such data would require automated tracking of hundreds of thousands of video frames—a goal we are working toward, but not yet achieved. Alternatively, additional on-line optical sensors could be installed to measure $\psi$ in real time.

Plot (B) in figure 3.9 examines the influence of wing shape by varying $\hat{r}_1$. As a result of different values of $\hat{r}_2$, we find that $\bar{C}_L$ increases as $\hat{r}_2$ increases, as expected. The power factor for $\hat{r}_1 = 0.45$ is not plotted because the power factor did not peak until above system resonance, so the rotational kinematics would be quite different and not comparable to the other cases. In retrospect, it would have been better to hold $\hat{r}_2$ constant and change $R$ for different values of $\hat{r}_1$. This would ensure the wings would develop their optimal performance with similar magnitudes of lift. If a softer wing hinge was used for the $\hat{r}_1 = 0.45$ wing, it would obtain a peak power factor at a

lower flapping frequency, but then the magnitudes of lift force and power consumption would be lower, reducing accuracy of the measurements.

These preliminary experiments have produced interesting results, but also uncovered several limitation to the current flapping experimental setup. The power calibration curves in figure 3.8-D should be straight lines—dielectric losses scale linearly with input frequency. However, there are resonances in the flapping device which cause deviations from this linear behavior. If the behavior of these modes is completely linear, then the calibration data will yield the correct power consumption. However, if the system is nonlinear, when a wing is installed and flapped, these extra modes may consume more or less power than predicted from the unloaded calibration at that particular frequency. Stiffer wing drivers are certainly in order.

There are also problems with stability of the capacitive force sensors. Each sensor probe is held by a two-axis angular positioning mount, allowing the probe and target plate to be aligned parallel to one another. Linear stages allow precision adjustment of the gap between sensor and target. However, these mounts are subject to creep and stiction, and occasionally the force measurements have small jumps or other problems. Next generation force sensors should remove all adjustment stages from the target-sensor force loop and "machine-in" the required alignment accuracy, for example by using precision-machined fixtures to hold the Invar sensor beam during laser welding.

We continue to have problems with wing hinge degradation. By using a discrete wing hinge, inertial and aerodynamic forces are concentrated at the hinge. It is also hypothesized that thermal effects are affecting results, due either to heating at the

wing hinge from repeated flexing, or heat generated by the actuator itself. Convective cooling from wing airflows may also affect force measurements. Thermocouple instrumentation of the drive actuator and sensor beam should be employed to diagnose these problems.

## 3.6 Discussion

There are several important results worth summarizing. When driven by linear (non-gearbox) actuators, a reduction in flapping frequency decreases actuator power density. This sets up a conflict between minimizing aerodynamic power and maximizing actuator power density. For fixed payload mass fraction, there is a fixed maximum wing length, independent of vehicle mass; endurance-maximizing designs will have a wing length half this maximum. For these designs, the battery mass fraction and actuator mass fraction will always be equal, no matter their respective energy densities. Using a motor and gearbox to drive the wings removes the upper limit on wing size, allowing high-mass designs that are not feasible when using linear actuators.

Wing inertia determines the maximum possible flapping frequency, which sets a lower bound on wing length and an upper bound on flight velocity. These bounds hold for both linear and motor actuators, but for linear actuators, finite wing inertia also leads to a limit on maximum vehicle mass. Physical reasoning and morphological insect data indicate that wing mass moment of inertia scales, roughly, as the product of wing radius to the fourth power and the square root of body/vehicle mass.

Opportunities for improvement and expansion of these models are manifold. If the type of actuator is known, then an improved model of power efficiency can be

included. For example, the low efficiency of piezoelectric actuators results primarily from dielectric losses; a loss model can replace the generic efficiency factor used here. If chemical or pneumatic actuators are used, the effect of time-varying mass can be included. Structural models and experimental data can replace the assumption of constant payload mass fraction. Payload models are easily modified to include known masses, such as processing and power electronics, sensors, and other fixed payloads.

Our conceptual design does not yet cover the control system. Many different control schemes are under active research, and clear winners have not yet emerged. The designer is forced to complete a detailed control system design before performing vehicle sizing. In time, the performance characteristics of the best control methods will be determined, and these data will provide preliminary mass and power estimates of the control system, allowing sizing and performance calculations to be performed before the detailed design phase.

Past the conceptual design phase, further refinements include detailed selection and modelling of flapping kinematics, transmission design, passive or active wing rotation design, wing testing and planform selection, and design and modelling of a vehicle control architecture; existing research on these topics is extensive.

It would be unwise to draw quantitative conclusions from any numerical results presented; for different actuator types and battery technologies, there is a large variation in energy density and efficiency—specifications which have a tremendous impact on system performance. In spite of this, the analytical results present clear design trends worthy of examination. MAVs driven by linear actuators are most appropriate for low-mass designs. As vehicle mass drops, there is greater flexibility in selecting

wing size, and flight endurance rises; fabrication limitations will set the minimum feasible size. As vehicle mass rises, at some point it becomes necessary to switch to motors. The precise cross-over mass—perhaps in the range of a few grams—depends on the efficiency and performance of available motors and linear actuators. Once the switch to motors is made, the designer must consider the advantages and disadvantages of moving to a helicopter design. It is not yet clear if flapping MAVs are faster or more maneuverable than their helicopter counterparts.

Flapping-wing MAVs show promising advantages, especially at the scale of small flying insects. Advances in fabrication and miniaturization continue to expand the feasible design space of these tiny vehicles, but the dependence of vehicle performance on design parameters is not always direct or intuitive. Designs must meet a range of competing performance requirements, such as size, payload, flight endurance, and speed. Optimizing indirect quantities, such as power consumption and lift, is an incomplete approach. Traditional aircraft conceptual design methods provide a model for balancing design requirements and optimizing performance. These ideas are easily and powerfully adapted to flapping-wing MAVs; useful not only for current designs, but in efficiently directing future research efforts to improve performance.

# Chapter 4

# Microfabrication

## 4.1 Introduction

Previous chapters have demonstrated the feasibility of all-axis control authority for insect-scale MAVs, sufficient lift to hover and maneuver, and adequate energy density of batteries and actuators for flight times on the order of minutes. Manufacturing challenges have forced the development of simplified designs and highly underactuated flapping mechanisms. As a result, these MAVs achieve only a very basic level of maneuverability, and in practice, stability margins are very slim. This stands in contrast to the amazing maneuverability and adaptability of actual insects. They are capable of complex aerial acrobatics as well as crawling and jumping behaviors. Future designs can only hope to develop this level of performance with more sophisticated mechanical designs, supported with many sensory inputs and multiple control actuators. Manufacturing techniques capable of providing this level of three-dimensional complexity and electromechanical integration in millimeter to centimeter-scale devices

did not previously exist.

Many machines realize greater performance and economy if made smaller. However, when shrunk to millimeter and micron sizes, new challenges arise in their construction. Monolithic fabrication must replace traditional methods, enabling efficient batch processing while eliminating the onerous assembly and handling of individual components. Integrated circuit technology has strongly influenced and informed this monolithic approach. Fabrication techniques include optical lithography, physical and chemical vapor deposition, spin coating of polymers, electroplating, thermal treatment, chemical and plasma etching, abrasive polishing and laser machining. Micro-devices with a variety of electrical and mechanical functions manufactured using these (and other) techniques are named microelectromechanical systems (MEMS). Many MEMS devices have found wide commercial success, including miniaturized accelerometers, gyroscopes, displays, electrical and optical switches, scanning mirrors and pressure sensors [24]. The success of these devices is due not only to the increased performance and reduced costs associated with miniaturization and batch fabrication, but to their tolerance of the limitations imposed by monolithic fabrication using integrated circuit techniques.

Most MEMS devices are made using surface micromachining [9]. Material is deposited onto a substrate, masked, and then etched. These steps are repeated to build up layers. As most methods of deposition are isotropic, chemical-mechanical polishing is often used to planarize each layer. Free-standing mechanical structures are created by removing sacrificial material or etching undercuts. When multiple materials are used, earlier layers must survive later deposition, etching, and thermal

treatment steps, potentially limiting the combinations of materials that can be used. Complex MEMS devices may have several material layers and require hundreds of sequential process steps. This highly serial nature compounds the impact of defects introduced at each step. To achieve economical device yields it is then necessary to reduce the number of layers and shrink the size of the individual devices. Most commercially successful MEMS devices are not hindered by a restriction to planar structures, material limitations, or increasing miniaturization. Indeed, many of the devices previously listed consist of a silicon structural element oscillating at high speed along a single axis. These requirements are well met by tiny, planar silicon components. Silicon has excellent specific stiffness and low thermal distortion, and processing methods are well-developed [31].

There is strong interest in constructing non-planar miniature devices that do not conform to traditional MEMS processing. Insect-scale MAVs, in particular, would be very challenging to make using surface micromachining. There are practical limitations on the types and thicknesses of material that can be deposited by vapor deposition, spin coating, and electroplating. It is not practical to use more than a few device layers. Bulk machining—a technique in which multiple substrates are machined separately and then bonded together—is an alternative MEMS process which eliminates the need for sequential planarization and allows layer substrates to be processed in parallel. Bulk machining enables thicker layers and allows for a wider range of layer materials. It has been used to create a variety of structurally complex miniature devices, including gas turbines [20], multi-axis force sensors [7], and microfluidic devices [1].

To overcome planar limitations inherent to MEMS, there have been many efforts to create three-dimensional structures through folding. Surface machined pin-and-staple hinges [32] and polymer flexures [42] are two common methods used to create folding linkages. Schemes to exploit deposition stresses [3] or solder/polymer surface tension during reflow [43] are common ways to induce folding. Co-fabricated assembly actuators [36], though bulky, allow for a highly controlled fold sequence. If latching mechanisms are present, stochastic assembly through simple agitation might also be used.

## 4.2 Smart Composite Microstructures

Work at Berkeley in support of the MFI project led to the development of the so-called smart composite microstructures (SCM) fabrication process [50]. These techniques were inspired, particularly, by previous work in folding MEMS. SCM was developed to create devices at MEMS-scale but with a wider range of materials, including high performance carbon fiber composites. It was also realized that flexure-based mechanisms avoid the unfavorable scaling of friction forces seen by sliding bearings as sizes shrink. An example MFI device is shown in figure 4.1. Each wing is driven by two actuators which are coupled to the wing through a spherical 5-bar transmission. This allows direct control over the flapping and pitching of the wing. Figure 4.2 illustrates the main concept behind SCM. The device is designed such that individual parts can be manufactured as rigid-flex laminates which are manufactured flat, and then folded up into "origami" components. These flexures are similar to those used on the wing hinge shown in figure 2.3. These flexure hinges in the rigid-

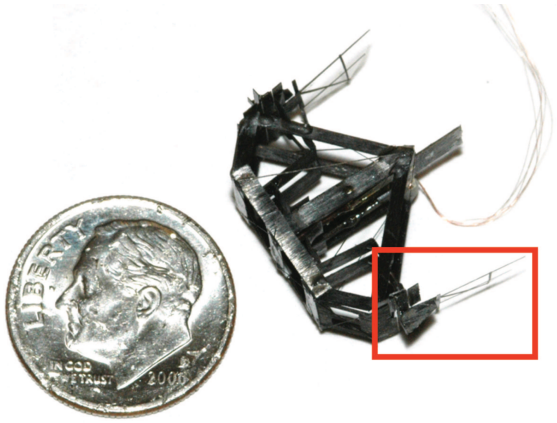

Figure 4.1: MFI prototype [18]. A spherical five-bar drive mechanism for one of the wings is highlighted.

flex laminate serve either as assembly fold-points or as mechanism flexures in the device.

Figure 4.3 illustrates the process of machining and laminating a 2D rigid-flex laminate. Laser machining and sequential lamination are used to build up the required layers. The rigid layers are made of unidirectional carbon fiber, pre-impregnated with an B-staged resin. During the bonding cycles, this resin is cured, adhering the rigid layers to adjacent flexible layers. Unfortunately, several problems plague this process. First, each layer of each part must be aligned by hand. These tiny parts are frequency only 1 millimeter or smaller in size, and each layer of each part must be handled individually and aligned under a microscope. There is also a tendency for the resin to flow into flexure gaps during bonding. A lower curing pressure relieves this problem, but at the expense of decreased bonding strength—rigid links frequently de-laminate.

Figure 4.4 is the result of an exercise to build the smallest flapping-wing MAV demonstration device possible with the SCM process. This device weighs only 8

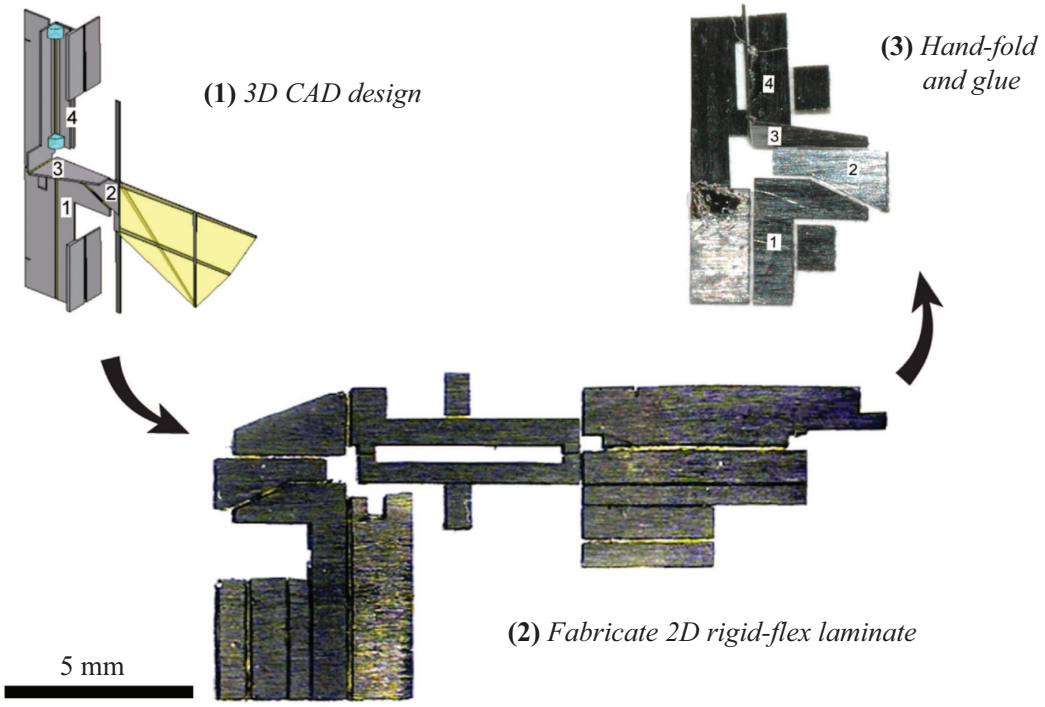


Figure 4.2: First, a 3D model of the part is constructed (A). Then, a scheme to flatten the 3D part into a 2D rigid-flex laminate is designed (B). After this part is manufactured, it is manually folded and glued into final form (C).

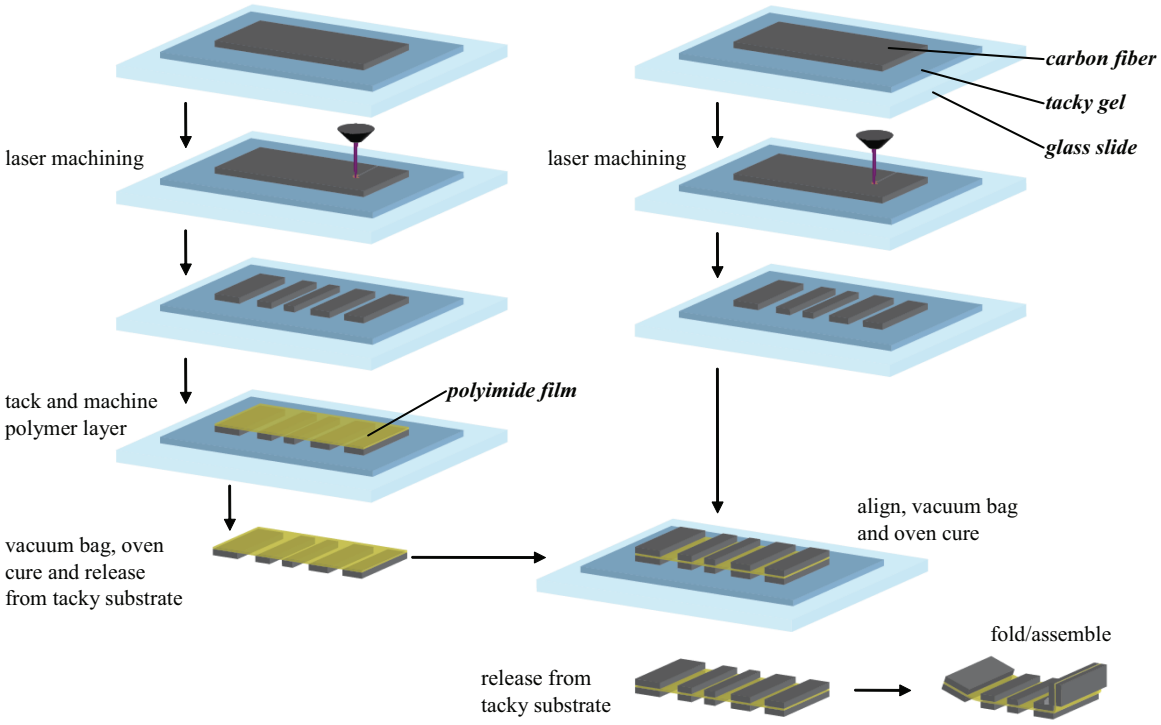


Figure 4.3: Process of making an SCM rigid-flex flat laminate.

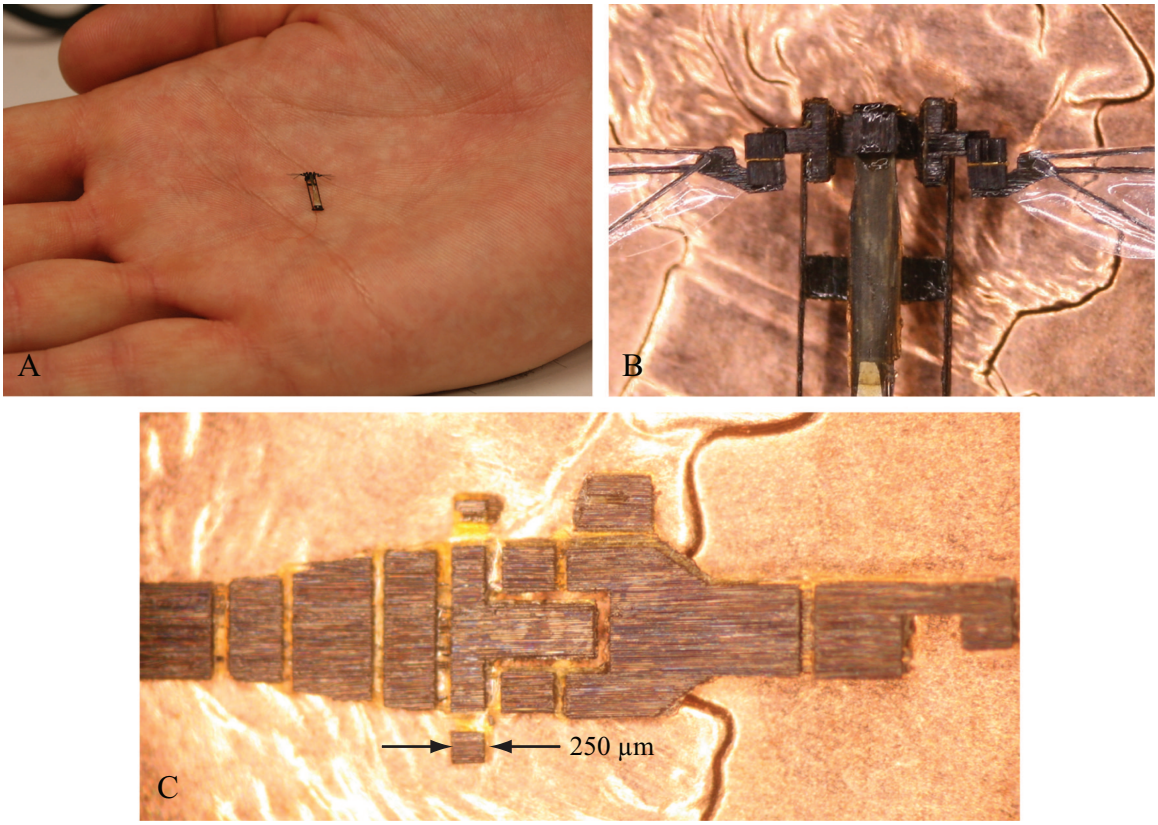


Figure 4.4: (A) An 8 milligram "micro-fly" demonstrator device. (B) Close-up of the transmission and wing hinges. (C) Transmission component prior to folding.

milligrams, flaps its wings at 600 Hz, and fits into a box only 10 millimeters on a side. Each part (actuator, airframe, wings (×2), wing hinges (×2), transmission) was fabricated separately and hand-assembled. The close-up view (B) clearly shows its "hand-crafted" character: misaligned and asymmetric parts, blobs of glue, etc. In (C) the transmission is shown pre-folding, and cutting debris and resin are clearly seen in the flexure gaps.

The SCM process, with great effort, can produce functional devices. However, the level of manual skill required is very high, and each device is slightly different and always asymmetrical. These problems not only extend the design cycle, but cause challenges when trying to operate and control devices in flight.

## 4.3 Printed-Circuit MEMS

To address the shortcomings of SCM fabrication, a new approach was developed, which has been named Printed Circuit MEMS (PC-MEMS). The name reflects the source of primary inspiration, the manufacture of high density rigid-flex printed circuit boards (PCBs). In particular, we have adopted adhesive bonding, mechanical layer alignment and parallel lamination—all common PCB fabrication methods.

Multilayer PCBs use precision dowel pins to maintain alignment during lamination. Alignment holes are punched or laser-drilled in each layer. The laminate is placed between precision die plates with relief holes for the alignment pins and then bonded in a heated press. Multiple layers are easily aligned and bonded simultaneously. Since mechanical alignment persists throughout the bonding cycle, misalignment from adhesive shearing and layer migration is largely eliminated. The challenges

of achieving high bond strength, low adhesive flow, and high accuracy alignment are well understood, and a wide array of highly optimized materials, tools and techniques are commercially available to support high-accuracy parallel lamination.

Our process, shown in figure 4.5, begins with the production of multilayer laminates. Individual layers are first bulk machined to define part geometry (A). Layers—post machining—must remain contiguous to preserve structural integrity of the layer and provide a stable mechanical connection from each device component to the alignment pins. Usual practice is to machine features while leaving small tabs or "bridges" connecting parts to the surrounding bulk material, similar to break-off tabs in panelized circuit boards. After lamination, a second round of machining, the "singulation" step, will free the individual parts. Any method of machining that is sufficiently accurate and compatible with the layer materials can be used. For our research purposes we use laser micromachining for its mask-less nature and compatibility with a wide range of materials. We employ a diode pumped Nd:$YVO_4$ laser, q-switched and frequency tripled to 355nm. Maximum average power is 1.5W, which we find sufficient for machining layers in the 1 to 150$\mu$m thickness range. The beam is focused to a spot approximately 8$\mu$m in diameter using a telecentric objective lens. Full-range accuracy and repeatability of beam/part positioning is 2$\mu$m or better.

After each layer is machined, optional steps—such as electropolishing, ultrasonic cleaning and plasma treatment—may be performed to prepare each layer for lamination. In flex circuit construction, circuit layers are usually bonded with acrylic sheet adhesives. PCB sheet adhesives are highly engineered materials with tailored thermal expansion properties, and they exhibit very little flow during the bonding cycle. We

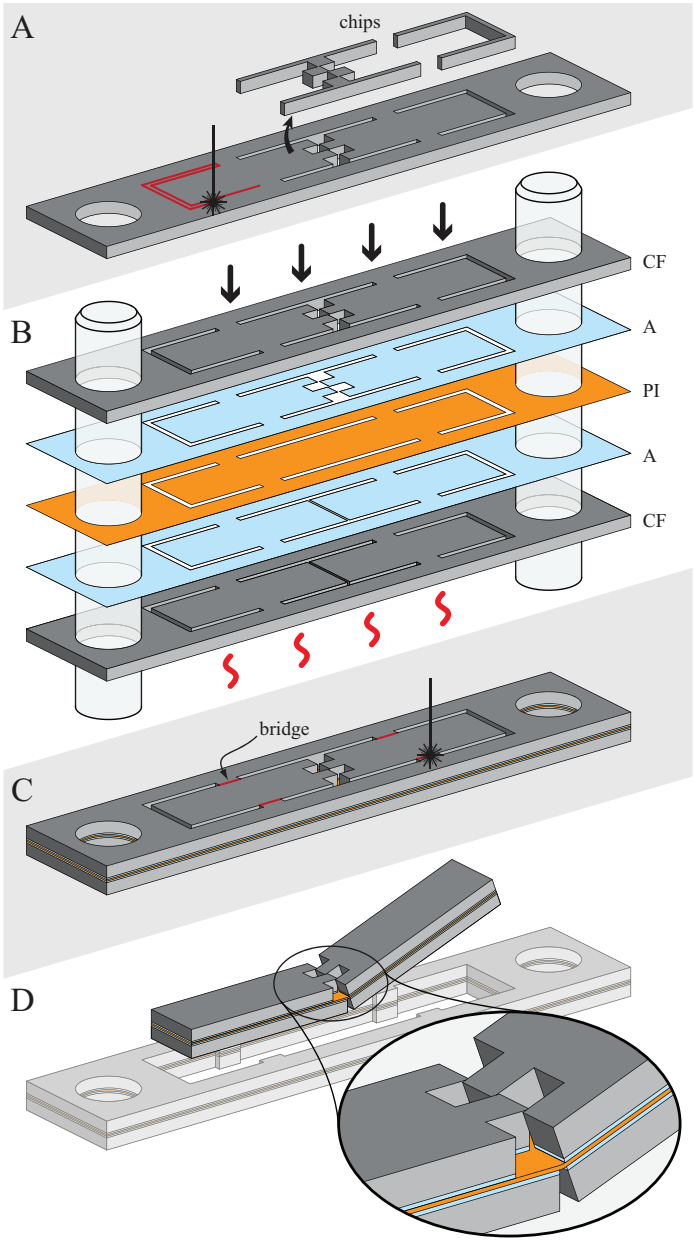


Figure 4.5: (A) machining of each laminate layer. (B) Layers are aligned using precision dowel pins and laminated in a heated press. (C) After lamination, devices are freed from the surrounding frame by a second machining pass. (D) The completed device is folded into shape.

use Dupont FR1500, a commercially-available acrylic sheet adhesive, 12.5$\mu$m thick. The adhesive is used in two ways; it is either machined with alignment holes and included as a free-standing layer, or it is tack-bonded to an adjacent layer. For either technique, laser machining is used to pattern the adhesive. Other adhesives or methods of adhesion could certainly be used, but we find the combination of properties present in this type to be suitable for our purposes.

After stacking the layers, the layup and tooling are placed in a heated press for bonding (B). The typical lamination cycle used was one hour at 190°C with 400kPa of pressure. Alignment accuracy is determined by several factors: alignment hole and pin accuracy, coefficients of thermal expansion for each layer material, bonding temperature, and the laminate dimensions. For alignment, we use precision dowel pins (1/16in); layer material permitting, alignment holes are undersized by a few microns to exploit elastic averaging. In practice, post-lamination alignment is better than 5$\mu$m. The exact accuracy is difficult to measure since the material uniformity and edge roughness of our current materials and machining process are of a similar scale.

SCM requires two lamination steps, and each layer for each part must be handled and aligned individually. In the PC-MEMS process, there is only one lamination step, and all layers are aligned mechanically rather than manually. Hundreds of parts can be manufactured in parallel without individual handling, similar to the "panelization" of PCBs. These techniques have dramatically improved the quality, accuracy, and uniformity of parts made. Fabrication time has been reduced from approximately one week to less than one day, dramatic increasing the number of designs and design

variations that may be explored.

## 4.4 Advanced PC-MEMS

These techniques have been advanced further still[1]. Now that alignment is achieved by mechanical means, it is feasible to laminate many layers together at once (up to 18 layers at once has been achieved). It is then possible to make very complicated structures akin to "pop-up books". Such complexity allows devices to be made out of fewer parts, each of greater complexity; in the extreme, devices may consist of a single part. Similarly, assembly degrees-of-freedom may be reduced, even down to one. Another advance is the replacement of manual gluing with reflow or wave soldering to freeze assembly degrees-of-freedom. Figure 4.6 gives a high-level overview of this advanced process and figure 4.7 shows several devices that have been manufactured using these techniques. A full account of these methods and devices are beyond the scope of this thesis, but may be found in references [48] and [41].

Previously, fabrication concerns have limited vehicles to very simple configurations. With clever design, it is possible to create vehicles with a very simplified mechanical design which can achieve basic stability and control. These new fabrication methods enable future designs which restore functionality and complexity, allowing the gap between MAV performance and insect performance to be closed. Advanced flapping and control mechanisms, integrated sensing, and greater maneuverability are all possible through advanced PC-MEMS and monolithic design.

[1]Expanded PC-MEMS methods were developed in collaboration with P. S. Sreetharan.

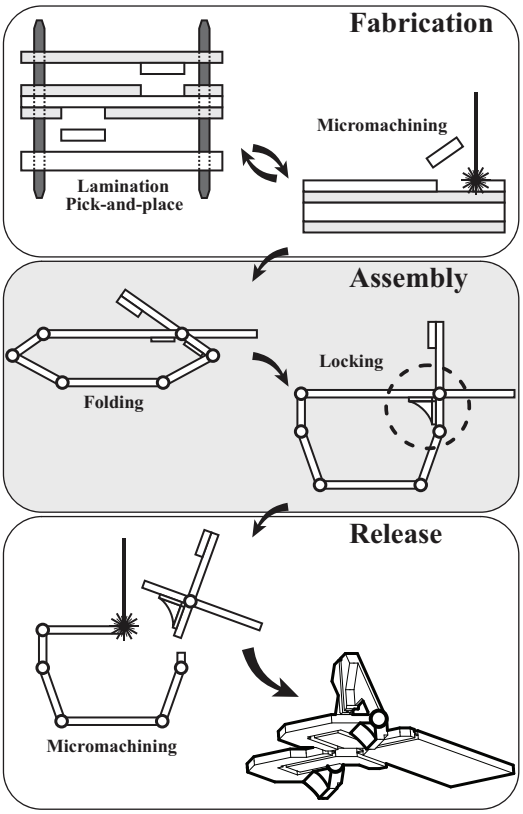


Figure 4.6: PC-MEMS has been extended to the creation of multi-level rigid-flex laminates. The most sophisticated devices consist of only one part which assembles with a single degree-of-freedom. This assembly degree-of-freedom is then fixed with a re-flow or wave soldering step, removing the need to manually glue parts together.

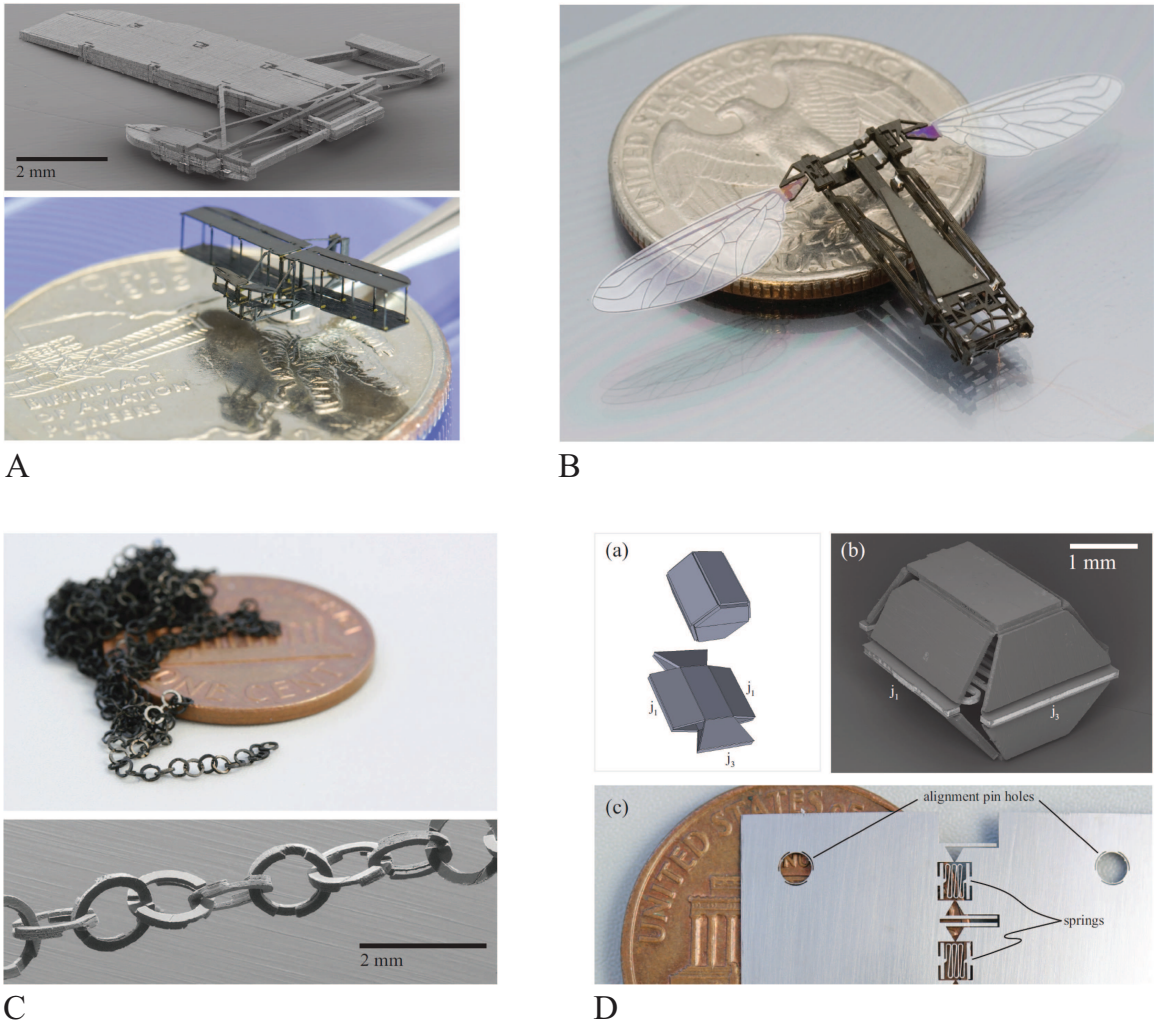


Figure 4.7: (A) 1:900 scale model of the 1903 Wright Flyer [48]. This device is laminated in one step, and folds with a single degree-of-freedom. Wing span is 14 millimeters and wing spars are 100$\mu$m by 100$\mu$m in cross-section. (B) A flapping-wing MAV which is laminated in two steps, assembles with a single degree-of-freedom, and is bonded with wave soldering, using the process shown in figure 4.6. A complete description is given in [41]. (C) A 500-link carbon fiber chain, manufactured monolithically with no assembly [48]. (D) This PC-MEMS device self-assembles through the use of a pre-strained elastic layer integrated into the laminate [48].

# Chapter 5

# Conclusions and Future Work

This thesis work was completed as part of a larger project at Harvard called the "Robobees" project. The goal of this project is, ostensibly, to create a colony of autonomous robotic bees tasked with pollinating a field of crops. However, this goal is really a framework to address several engineering challenges in low-power computation, battery and fuel-cell technology, microfabrication, etc. Future work arising from this thesis will be directed toward supporting the Robobees project and meeting its remaining challenges. In particular, the development of a high-performance control scheme is currently under investigation. This thesis established the feasibility of a passively-rotating split-cycle control strategy, and current work aims to understand the real-world performance of such a scheme through free-flight stability and control experiments. In fact, recent work indicates that the ability of the wings to effect sufficient control torques may be a more important topic of research than maximizing aerodynamic efficiency. Wings with greater compliance may be more suited to this task, and at-scale testing is essential to investigating flexible wings. To

this end, the clearest path forward from this thesis work is to improve wing testing facilities, allowing not only the testing of a wing in steady state, but the integration of candidate control mechanisms. Improving models of passive wing dynamics will likely require the measurement of wing moments as well as forces. Ideally a six-component force-torque sensor, sufficiently miniature, can be developed.

Upgrading testing facilities to more precisely control wing kinematics and more easily isolate inertial and aerodynamic force effects is highly desirable. Testing in high density gases (such as sulfur hexafluoride—approximately five times denser than air) reduces inertial forces and allows an easier investigation of aerodynamic forces and moments in isolation. Flapping frequencies are reduced for the same force level, and a wider range of wing Reynolds number can be tested as well. It would also be very useful, for the purposes of testing, to control wing rotation directly with a separate actuator and a spherical 5-bar transmission. However, this will add mass to the wing driver, reducing the bandwidth of the force sensor, so this type of testing may only make sense for high-density gas testing.

Lacking full direct control over wing rotation, the addition of on-line measurement of wing rotation is highly desirable. This would allow wing tests to control more easily for variations in wing kinematics, and would also allow closed-loop control (albeit underactuated) of wing rotation. As our ability to employ automatic tracking of wing features in high-speed video improves, it will become much easier to study compliant wings and extract measurements of wing twist and camber. Such measurements are very useful for testing different control strategies as well for improving hover efficiency.

Improvement of conceptual design methods can occur in a few areas. In practice,

we find that wings are limited not only by flexibility, but also by stress and fatigue at the wing root. The current methods also make no accounting for the impact of wing aspect ratio on flapping limits. It would also be interesting to carry this work further with respect to real insect wings. If wing stiffness can be measured along with wing inertia, then it is possible to characterize their structural-inertial efficiency independent of the choice of acceptable deflection. Further reductions in wing inertia will certainly expand the space of feasible designs, and can also improve wing testing by reducing inertial loads. Further reductions will most likely require investigation of manufacturing methods which can produce corrugated wings; there is little room remaining for material improvements.

The most immediately successful outcome of this thesis has been the improved manufacturing process. These techniques are under active development for new applications outside of microrobotics, including applications in micro-surgery, micro-optomechanics, and other millimeter-scale machines in many other fields. Future devices will have much tighter integration of electrical and mechanical components using PCB materials and methods. There is a strong analogy between integration of PCB methods and PC-MEMS and the integration of CMOS with surface-micromachined MEMS. The clear path toward economical mass production of Robobee devices is a feature shared by any new applications for PC-MEMS.

# Bibliography


[1] M. Agirregabiria, FJ Blanco, J. Berganzo, MT Arroyo, A. Fullaondo, K. Mayora, and JM Ruano-López. Fabrication of su-8 multilayer microstructures based on successive cmos compatible adhesive bonding and releasing steps. *Lab Chip*, 5(5):545–552, 2005.

[2] A. Andersen, U. Pesavento, and Z. J. Wang. Unsteady aerodynamics of fluttering and tumbling plates. *J. Fluid Mech.*, 541:65–90, 2005.

[3] W.J. Arora, A.J. Nichol, H.I. Smith, and G. Barbastathis. Membrane folding to achieve three-dimensional nanostructures: Nanopatterned silicon nitride folded with stressed chromium hinges. *Applied physics letters*, 88(5):053108–053108, 2006.

[4] M.F. Ashby. *Materials selection in mechanical design*. Butterworth-Heinemann, 2005.

[5] A. J. Bergou, S. Xu, and Z. J. Wang. Passive wing pitch reversal in insect flight. *J. Fluid Mech.*, 591:321–337, 2007.

[6] G. J. Berman and Z. J. Wang. Energy-minimizing kinematics in hovering insect flight. *J. Fluid Mech.*, 582:153–168, 2007.

[7] F. Beyeler, S. Muntwyler, and B.J. Nelson. A six-axis mems force–torque sensor with micro-newton and nano-newtonmeter resolution. *Microelectromechanical Systems, Journal of*, 18(2):433–441, 2009.

[8] J.-Y. Bouguet. Camera Calibration Toolbox for Matlab. `http://www.vision.caltech.edu/bouguetj/calib_doc/`, 2008.

[9] J.M. Bustillo, R.T. Howe, and R.S. Muller. Surface micromachining for microelectromechanical systems. *Proceedings of the IEEE*, 86(8):1552–1574, 1998.

[10] T.L. Daniel and S.A. Combes. Flexing wings and fins: bending by inertial or fluid-dynamic forces? *Intgr. and Comp. Biol.*, 42(5):1044–1049, 2002.

[11] M. H. Dickinson, F.-O. Lehmann, and S. P. Sane. Wing rotation and the aerodynamic basis of insect flight. *Science*, 284:1954–1960, 1999.

[12] W. B. Dickson, A. D. Straw, C. Poelma, and M. H. Dickinson. An integrative model of insect flight control. In *Proc. AIAA Aerospace Sciences Meeting and Exhibit*, Reno, NV, January 2006.

[13] D. B. Doman and M. W. Oppenheimer. Dynamics and control of a minimally actuated biomimetic vehicle: Part-I aerodynamic model. In *Proc. AIAA Guid. Nav. Cont. Conf.*, San Francisco, CA, August 2009.

[14] R. Dudley. *The biomechanics of insect flight: form, function, evolution*. Princeton University Press, 2000.

[15] C. P. Ellington. The aerodynamics of insect flight. II. Morphological parameters. *Phil. Trans. R. Soc. Lond.* B, 305:17–40, 1984.

[16] A.R. Ennos. The importance of torsion in the design of insect wings. 140:137–160, 1988.

[17] A.R. Ennos. The inertial cause of wing rotation in Diptera. 140:161–169, 1988.

[18] R. S. Fearing, K. H. Chiang, M. H. Dickinson, M. H. Pick, D. L. Sitti, and J. Yan. Wing transmission for a micromechanical flying insect. In *Proc. IEEE Int. Conf. Rob. Autom.*, San Francisco, CA, April 2000.

[19] B.M. Finio, N.O. Pérez-Arancibia, and R.J. Wood. System identifcation and linear time-invariant modeling of an insect-sized flapping-wing micro air vehicle. In *Intelligent Robots and Systems (IROS), 2011 IEEE/RSJ International Conference on*, pages 1107–1114. IEEE.

[20] L.G. Fréchette, S.A. Jacobson, K.S. Breuer, F.F. Ehrich, R. Ghodssi, R. Khanna, C.W. Wong, X. Zhang, M.A. Schmidt, and A.H. Epstein. High-speed microfabricated silicon turbomachinery and fluid film bearings. *Microelectromechanical Systems, Journal of*, 14(1):141–152, 2005.

[21] S. N. Fry, R. Sayaman, and M. H. Dickinson. The aerodynamics of free-flight maneuvers in drosophila. *Science*, 300:495–498, 2003.

[22] C. Graetzel. *MEMS & High Speed Vision: Development and Application to Reverse-engineer Drosophila Flight Control*. PhD thesis, ETH Zurich, 2008.

[23] C. F. Graetzel, S. N. Fry, F. Beyeler, Y. Sun, and B. J. Nelson. Real-time microforce sensors and high speed vision system for insect flight control analysis. In *Exp. Robotics: The 10th Int. Symp. on Exp. Robotics*, page 451. Springer Verlag, 2008.

[24] J.W. Judy. Microelectromechanical systems (mems): fabrication, design and applications. *Smart materials and Structures*, 10:1115, 2001.

[25] M. Karpelson, J.P. Whitney, G.Y. Wei, and R.J. Wood. Energetics of flapping-wing robotic insects: towards autonomous hovering flight. In *Intelligent Robots and Systems (IROS), 2010 IEEE/RSJ International Conference on*, pages 1630–1637. IEEE.

[26] M. Keennon, K. Klingebiel, H. Won, and A. Andriukov. Development of the nano hummingbird: A tailless flapping wing micro air vehicle. In *50th AIAA Aerospace Sciences Meeting*, volume 0588, 2012.

[27] J.G. Leishman. *Principles of helicopter aerodynamics*. Cambridge Univ Pr, 2006.

[28] D. Lentink and M.H. Dickinson. Rotational accelerations stabilize leading edge vortices on revolving fly wings. *Journal of Experimental Biology*, 212(16):2705, 2009.

[29] D. Lentink, S.R. Jongerius, and N.L. Bradshaw. The scalable design of flapping micro-air vehicles inspired by insect flight. *Flying Insects and Robots*, page 185, 2009.

[30] N.O. Pérez-Arancibia, K.Y. Ma, K.C. Galloway, J.D. Greenberg, and R.J. Wood. First controlled vertical flight of a biologically inspired microrobot. *Bioinspiration & Biomimetics*, 6:036009, 2011.

[31] K.E. Petersen. Silicon as a mechanical material. *Proceedings of the IEEE*, 70(5):420–457, 1982.

[32] K.S.J. Pister, MW Judy, SR Burgett, and R.S. Fearing. Microfabricated hinges. *Sensors and Actuators A: Physical*, 33(3):249–256, 1992.

[33] T.N. Pornsin-Sirirak, Y.C. Tai, C.M. Ho, and M. Keennon. Microbat: A palm-sized electrically powered ornithopter. In *Proceedings of NASA/JPL Workshop on Biomorphic Robotics*, pages 14–17, 2001.

[34] S.S. Rao. *Mechanical vibrations*. Addison-Wesley New York, 1990.

[35] D.P. Raymer, American Institute of Aeronautics, and Astronautics. *Aircraft design: a conceptual approach*. American Institute of Aeronautics and Astronautics Reston, VA, 2006.

[36] J.R. Reid, V.M. Bright, and JT Butler. Automated assembly of flip-up micromirrors. *Sensors and Actuators A: Physical*, 66(1-3):292–298, 1998.

[37] L. Ristroph, G. J. Berman, A. J. Bergou, Z. J. Wang, and I. Cohen. Automated hull reconstruction motion tracking (hrmt) applied to sideways maneuvers of free-flying insects. 212(9):1324, 2009.

[38] S. P. Sane. The aerodynamics of insect flight. 206(23):4191, 2003.

[39] S. P. Sane and M. H. Dickinson. The aerodynamic effects of wing rotation and a revised quasi-steady model of flapping flight. *J. Exp. Biol.*, 205:1087–1096, 2002.

[40] L. I. Sedov. *Two-dimensional problems in hydrodynamics and aerodynamics.* Interscience Publishers, 1965.

[41] Sreetharan, P. and Whitney, J.P. and Strauss, M. and Wood, R.J. Monolithic fabrication of millimeter-scale machines. *J. Micromech. Microeng.*, 2012.

[42] K. Suzuki, I. Shimoyama, H. Miura, and Y. Ezura. Creation of an insect-based microrobot with an external skeleton and elastic joints. In *Micro Electro Mechanical Systems, 1992, MEMS'92, Proceedings. An Investigation of Micro Structures, Sensors, Actuators, Machines and Robot. IEEE*, pages 190–195. IEEE, 1992.

[43] R.R.A. Syms, E.M. Yeatman, V.M. Bright, and G.M. Whitesides. Surface tension-powered self-assembly of microstructures-the state-of-the-art. *Microelectromechanical Systems, Journal of*, 12(4):387–417, 2003.

[44] H. Tanaka, K. Hoshino, K. Matsumoto, and I. Shimoyama. Flight dynamics of a butterfly-type ornithopter. *In Proc. IEEE/RSJ Int. Conf. on Intelligent Robots and Systems*, pages 2706–2711, 2005.

[45] H. Tanaka, J.P. Whitney, and R.J. Wood. Effect of flexural and torsional wing flexibility on lift generation in hoverfly flight. *Integrative and Comparative Biology*, 51(1):142, 2011.

[46] S. M. Walker, A. L. R. Thomas, and G. K. Taylor. Photogrammetric reconstruction of high-resolution surface topographies and deformable wing kinematics of tethered locusts and free-flying hoverflies. *J. of The Royal Society Interface*, 6(33):351, 2009.

[47] Z. J. Wang. Two dimensional mechanism for insect hovering. *Phys. Rev. Lett.*, 85(10), 2000.

[48] JP Whitney, PS Sreetharan, KY Ma, and RJ Wood. Pop-up book MEMS. *Journal of Micromechanics and Microengineering*, 21(11):115021–115027, 2011.

[49] R. J. Wood. The first takeoff of a biologically inspired at-scale robotic insect. *IEEE Trans. Rob.*, 24:341–347, 2008.

[50] R. J. Wood, S. Avadhanula, R. Sahai, E. Steltz, and R. S. Fearing. Microrobot Design Using Fiber Reinforced Composites. *J. Mech. Design*, 130:52304–52315, 2008.

[51] R. J. Wood, E. Steltz, and R. S. Fearing. Nonlinear performance limits for high energy density piezoelectric bending actuators. In *Proceedings of the 2005 IEEE International Conference on Robotics and Automation (ICRA)*, pages 3633–3640. IEEE, 2005.

[52] RJ Wood, KJ Cho, and K. Hoffman. A novel multi-axis force sensor for microrobotics applications. *Smart Materials and Structures*, 18:125002, 2009.

[53] J. H. Wu and M. Sun. Unsteady aerodynamic forces of a flapping wing. *J. Exp. Biol.*, 207:1137–1150, 2004.

[54] C. S. Yih. *Fluid mechanics: a concise introduction to the theory*. West River Press, 1977.

[55] J. Young, S.M. Walker, R.J. Bomphrey, G.K. Taylor, and A.L.R. Thomas. Details of insect wing design and deformation enhance aerodynamic function and flight efficiency. *Science*, 325(5947):1549–1552, 2009.

[56] Z. Zhang. A flexible new technique for camera calibration. 22(11):1330–1334, 2000.